JGR Oceans

RESEARCH ARTICLE

10.1029/2025JC022718

Biophysical Interactions Stimulate the Spring Phytoplankton Bloom in the North Pacific Subtropical Recirculation Gyre

Chiho Sukigara[1], **Ryuichiro Inoue**[1], **Kanako Sato**[1], **Yoshihisa Mino**[2], **Takeyoshi Nagai**[3], **Andrea J. Fassbender**[4,5], **Yuichiro Takeshita**[5], **and Eitarou Oka**[6]

[1]Japan Agency for Marine-Earth Science and Technology, Yokosuka, Japan, [2]Institute for Space-Earth Environmental Research, Nagoya University, Nagoya, Japan, [3]Tokyo University of Marine Science and Technology, Tokyo, Japan, [4]NOAA/OAR Pacific Marine Environmental Laboratory, Seattle, WA, USA, [5]Monterey Bay Aquarium Research Institute, Moss Landing, CA, USA, [6]Atmosphere and Ocean Research Institute, The University of Tokyo, Kashiwa, Japan

Key Points:

- Phytoplankton biomass in the N. Pacific subtropical gyre increased significantly in the restratified surface layer just after deep mixing
- In the frontal area, the water column rapidly restratified via horizontal rearrangement of water masses after mixing
- Horizontal rearrangement of water masses caused nutrient-rich, twilight zone water to be entrained to near the euphotic zone

Supporting Information:

Supporting Information may be found in the online version of this article.

Correspondence to:

C. Sukigara,
sukigarac@jamstec.go.jp

Citation:

Sukigara, C., Inoue, R., Sato, K., Mino, Y., Nagai, T., Fassbender, A. J., et al. (2025). Biophysical interactions stimulate the spring phytoplankton bloom in the North Pacific subtropical recirculation gyre. *Journal of Geophysical Research: Oceans*, *130*, e2025JC022718. https://doi.org/10.1029/2025JC022718

Received 4 APR 2025
Accepted 7 JUL 2025

Author Contributions:

Data curation: Kanako Sato
Formal analysis: Chiho Sukigara
Funding acquisition: Ryuichiro Inoue, Takeyoshi Nagai, Andrea J. Fassbender, Yuichiro Takeshita, Eitarou Oka
Investigation: Chiho Sukigara, Ryuichiro Inoue, Takeyoshi Nagai, Andrea J. Fassbender, Yuichiro Takeshita, Eitarou Oka
Methodology: Yoshihisa Mino
Supervision: Eitarou Oka
Validation: Ryuichiro Inoue, Kanako Sato
Visualization: Chiho Sukigara, Ryuichiro Inoue

Abstract Although previous studies have found that restratification caused by mixed layer eddies induces early spring blooms near fronts under the nutrient-replete conditions of the subarctic ocean, the genesis of the spring bloom in nutrient-depleted subtropical regions has been unclear. To investigate the biogeochemical responses to changes of ocean dynamics during the spring transition season in the oligotrophic subtropical gyre of the western North Pacific from January to April of 2018, we used two Biogeochemical Argo floats equipped with oxygen, fluorescence (to estimate chlorophyll concentrations), backscatter (to estimate the concentration of particulate organic carbon [POC]), and nitrate and nitrite sensors to collect daily vertical profiles of the water column from a depth of 2,000 m to the sea surface. During February and March, as the mixed layer gradually deepened, there were slight increases of the concentrations of chlorophyll and POC after temporary restratification. At the end of March, the depth of the mixed layer reached a maximum, and the water column rapidly stratified. Chlorophyll concentrations increased significantly in the surface water, and low-salinity water with high concentrations of nutrients and low concentrations of oxygen and POC apparently entered the subsurface layer from greater depths. We hypothesize that this vertical structure was created by ageostrophic secondary circulation in frontal areas that enhanced the upward transport of nutrients into the euphotic zone and resulted in rapid phytoplankton growth in the surface layer as the light environment improved.

Plain Language Summary In subtropical areas where nutrient concentrations are low in surface waters, the supply of nutrients from deeper water by deep winter mixing has been thought to cause spring phytoplankton blooms after warming causes the water column to restratify. However, the relationship between restratification and phytoplankton blooms is still under debate because the relevant phenomena have been difficult to observe. In this study, two autonomous profiling floats with temperature, salinity, and pressure sensors as well as dissolved oxygen, nitrate and nitrite, chlorophyll, and backscatter sensors were deployed in the subtropical region of the western North Pacific from January to April 2018. The results revealed restratification and high chlorophyll concentrations in the surface layer (0–20 m) within a few days after the depth of the mixed layer reached a maximum in late March. Water with high nutrient concentrations and low oxygen concentrations was transported into the subsurface layer (20–100 m) from greater depths. These phenomena were hypothesized to have been caused by a mechanism called secondary circulation and resulted in higher primary production than would be associated with the traditional formation of a deep mixed layer in the winter followed by restratification during the spring.

1. Introduction

The North Pacific Subtropical Gyre (NPSG) is a convergence zone considered to have low biological productivity because the nutrient concentrations and phytoplankton biomass in the euphotic zone are lower than highly productive ocean regions (Chavez et al., 2011; Irwin & Oliver, 2009). However, phytoplankton concentrations increase when nutrients at depth are entrained into the surface sunlit area during deepening of the mixed layer by winter cooling and strong winds (Siegel et al., 2002; Siswanto et al., 2015). Initiation of this “spring bloom” has been examined in many studies. The critical depth hypothesis (Sverdrup, 1953) argues that nutrients are supplied to the euphotic zone as the mixed layer deepens, and subsequent warming causes shoaling of the mixed layer and improved light conditions that stimulate phytoplankton growth, which can exceed respiration in the mixed layer once a critical mixed layer depth is reached. However, discrepancies of the timing of mixed layer shoaling and

Writing – original draft: Chiho Sukigara
Writing – review & editing: Ryuichiro Inoue, Kanako Sato, Yoshihisa Mino, Takeyoshi Nagai, Andrea J. Fassbender, Yuichiro Takeshita

increases of chlorophyll concentrations, an indicator of phytoplankton growth, have been reported (Chiswell, 2011). Taylor and Ferrari (2011) have argued that phytoplankton blooms can occur during winter, despite a deep mixed layer, if the turbulence is sufficiently weak that phytoplankton can accumulate in the upper, sunlit portion of the water column (the critical turbulence hypothesis). Behrenfeld (2010) has argued that dilution of the predation pressure of zooplankton on phytoplankton by mixing can initiate a bloom even if mixing is deep (the dilution-recoupling hypothesis). Although various hypotheses about phytoplankton blooms have been proposed (Fischer et al., 2014), the factors that determine the timing and magnitude are not fully understood. One reason for this lack of understanding maybe the inadequacy of data sets that could reveal the physical and biological processes associated with bloom development. In particular, the paucity of in situ nutrient data has limited understanding of phytoplankton growth in the NPSG. Biogeochemical profiling floats equipped with nitrate sensors (Johnson et al., 2010) are now providing important clues that facilitate understanding of bloom development processes.

In recent years, phytoplankton blooms associated with three-dimensional (3D) circulation, which cannot be explained by a one-dimensional (1D) mixing and restratification process, have been studied with high-resolution spatiotemporal data sets that have included measurements from satellites, autonomous profiling floats (e.g., Argo floats), and self-propelled, buoyancy-driven autonomous underwater vehicles (e.g., underwater gliders). Mahadevan et al. (2012) have shown that the spring phytoplankton bloom observed south of Iceland in the subpolar North Atlantic starts earlier in frontal regions, where it is initiated by restratification caused by cyclonic eddies in the mixed layer, than in nonfrontal regions, where restratification occurs by seasonal warming of the surface water. The 3D circulation in mixed layer eddies and fronts (Fox-Kemper et al., 2008) and the subsequent phytoplankton responses on smaller temporal (a few days to a few weeks) and spatial (a few km to a few tens of km) scales have been studied using data measured by floats equipped with biogeochemical sensors (McKee et al., 2023; Zhang et al., 2019).

The northwestern region of the NPSG is an area of low-nutrient concentrations with a maximum nitrate concentration of about 1 μmol L^{-1} in the surface layer even in winter (Honda et al., 2017; Wakita et al., 2016). However, seasonally repeated shipboard measurements (October–November 2010, February–March, April, July 2011) conducted in both the oligotrophic subtropical region south of the Kuroshio Extension and the eutrophic subarctic region to the north have revealed higher chlorophyll concentrations and primary productivity in the subtropics during February (Fujiki et al., 2016; Matsumoto et al., 2016). Matsumoto et al. (2021) have explained that the high productivity at this time results from nutrient transport into surface waters by deep winter mixing. This explanation contradicts the common scenario because primary productivity increased despite the deep mixing and exceeded the primary productivity in other eutrophic areas such as the subarctic Pacific, even in the relatively low-nutrient environment of the NPSG. However, because of the high spatiotemporal variability within the NPSG, the spatiotemporal extent of the high primary production within the NPSG is unclear. Furthermore, details of the processes that lead from the supply of nutrients via mixing to increased primary productivity have not been well described in previous studies. The northwestern part of the NPSG is a region with a complex structure that is intermediate between subtropical water and Kuroshio water and is affected by the Kuroshio Current, the Kuroshio Extension, and abundant mesoscale and submesoscale eddies. The resolution of conventional shipboard snapshot observations may therefore be too coarse to resolve and understand biogeochemical processes that occur there. Detailed analysis of phytoplankton blooms in this area requires observations with higher spatiotemporal resolution than can be provided by shipboard observations.

In this study, data from two floats equipped with biogeochemical sensors, satellite data (sea surface height and ocean color), and shipboard data (mainly as validation data for the float sensors) were combined to observe variations of physical properties and biological processes from winter (late January) to spring (late April) in the region of formation of North Pacific subtropical mode water. The unique feature of this study was that not only chlorophyll and backscatter sensors but also oxygen and nutrient sensors were mounted on the floats, and the accuracies of the float data were assured by comparing the float data with the shipboard observations at stations where floats were deployed and retrieved. The two floats were no more than 20 km apart and made daily observations. The notable differences between the profiles obtained by these floats on the same day suggested that the floats were in an area of large horizontal variability. The objective of this study was to clarify how changes of the structure of the water column influenced nutrient availability and biological activity during the spring transition by using a combination of float, shipboard, and satellite data sets as well as simulations by a numerical model. We explain the shipboard and float observations and the methods of correcting the float biogeochemical

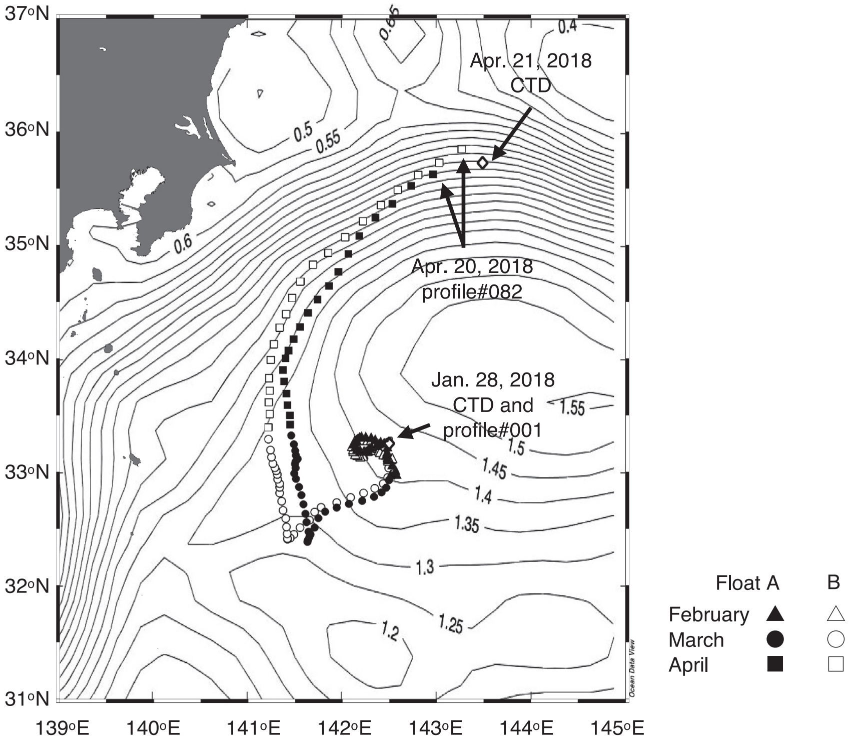

Figure 1. Map of the study area showing the two Argo float trajectories (closed triangles, circles, and squares: Argo 2903329 [Float A]; open triangles, circles, and squares: Argo 2903330 [Float B]) and the *R/V Shinsei-maru* CTD stations where water samples were collected (diamonds). Float positions in February, March, and April are indicated by triangles, circles, and squares, respectively. The background contours show absolute dynamic topography for the float observation period.

sensors in Section 2, the results of the float observations in Section 3, the temporal changes of the structure of the water column and the biogeochemical responses over the entire observation period in Section 4.1, and the mechanism that explained the occurrence of the significant increase of chlorophyll observed in late March in Section 4.2.

2. Materials and Methods

2.1. Float Observations

On 28 January 2018, during cruise KS-18-1 of the R/V Shinsei-Maru (18–30 January 2018), two Navis Biogeochemical (BGC) autonomous profiling (Argo) floats (Sea-Bird Scientific, USA: World Meteorological Organization nos. 2903329 and 2903330) were launched at 33.25°N, 142.50°E in the Kuroshio recirculation gyre south of the Kuroshio Extension (Figure 1). The floats moved along small clockwise trajectories around 33°N, 142°E for approximately one month and then moved southwest for two weeks until mid-March. During most of this time, the two floats were within 10 km of each other. Around 14 March, the floats turned north from their southernmost location of 32.42°N, and float WMO2903329 (Float A) remained east of float WMO2903330 (Float B) until recovery. After 6 April, the direction of the floats changed to the northeast, and their speed increased. The floats were recovered on 21 April 2018 during cruise KS-18-4 of the R/V Shinsei-Maru (from 20 April to 1 May 2018).

Each float was programmed to profile daily, to reach the sea surface at 12:00–14:00 UTC (21:00–23:00 local time), and to remain there for about 15 min to transmit data via the Iridium satellite-based wireless communication system before returning to its parking depth. Each float was equipped with an SBE41CP conductivity-temperature-depth (CTD) sensor (Sea-Bird Electronics, Inc., Bellevue, USA). After descending from a parking depth of 1,000 dbar to a depth of 2,000 dbar, the floats measured CTD data (vertical sampling intervals: every 2 dbar between 0 and 500 dbar, every 4 dbar between 500 and 1,000 m, and every 8 dbar between 1,000 and 2,000 dbar) during their ascent to the sea surface. The depth of the mixed layer (Z_m) in this study was defined to be the shallowest depth at which the density was 0.03 kg m^{-3} greater than the density at the sea surface, which was defined to be the average density of the shallowest observed layer above at most 10 dbar (de Boyer Montégut et al., 2004).

The floats were also equipped with an optical dissolved oxygen (DO) sensor (SBE63), a nitrate plus nitrite (N + N) sensor (DeepSUNA), and a sensor that measured chlorophyll fluorescence, 700-nm optical backscatter, and fluorescent dissolved organic matter (MCOMS, WETLabs, USA). All sensors except the N + N sensor made observations at the same depths as the CTD. The N + N sensor, unlike the other sensors, had a coarse vertical sampling resolution (every 4 dbar between 0 and 130 dbar, every 30 dbar between 130 and 400 dbar, and every 50 dbar between 400 and 2,000 dbar). Profiled data measured by Argo floats in this paper are available at the websites of the Global Data Assembly Centers: https://usgodae.org/pub/outgoing/argo and https://data-argo.ifremer.fr (Argo, 2000).

2.2. Shipboard Observations

The discrete observations reported here were collected during cruises KS-18-1 and KS-18-4 of the R/V Shinsei-maru. Ship-based sampling was performed using a rosette equipped with 24 12-L Niskin bottles, a 9PLUS CTD sensor, and an SBE43 oxygen sensor (Sea-Bird Scientific, USA). We collected CTD observations from 2,000 m to the sea surface at the location of deployment (33.25°N, 142.5°E; station C005 during cruise KS-18-1) of both BGC-Argo floats and at the recovery location (35.72°N, 143.49°E; station C002 during cruise KS-18-4) of Float B (Figure 1). Water samples for salinity and concentrations of nutrients, DO, chlorophyll *a*, and particulate organic carbon (POC) were collected to calibrate sensors on the shipboard CTD and floats. During cruise KS-18-1, the CTD was equipped with a photosynthetically active radiation (PAR) sensor (LI-COR Biospherical PAR sensor, Biospherical Instruments, Inc., USA) to measure light in the water column.

2.3. Correction of Float Data

2.3.1. Dissolved Oxygen and Nutrients

The DO concentrations in sampled water were measured with an onboard titration unit (MPT Titrino 798: Metrohm, Japan) with the Winkler method (Japan Meteorological Agency, 1999) and used to calibrate an SBE43 oxygen sensor. The DO saturation was calculated from the estimated saturated DO concentration using water temperature and salinity (Garcia & Gordon, 1992), and the measured DO concentration. The water samples for measurements of nitrate concentrations were immediately frozen at −20°C and kept in a freezer until the nutrient concentrations were measured with an autoanalyzer (QuAAtro: BL Tec, Japan). The total concentration of nitrate plus nitrite (N + N) was determined by reducing nitrate to nitrite over a cadmium-copper reduction column and was measured based on the absorption of an azo dye at a wavelength of 550 nm (Grasshoff, 1976).

The outputs of the DO sensors on the floats were first converted to oxygen concentrations following the standard protocols outlined in Thierry et al. (2018) using adjusted salinity data based on Wong and Keeley. (2020). Oxygen concentrations from the first profile of each float were compared with CTD observations made at the time the float was deployed. A linear regression between float and CTD values from a region of the water column in which the oxygen gradient was less than 0.2 μmol O_2 kg^{-1} $dbar^{-1}$ was used to determine the gain of the float sensor (Takeshita et al., 2013). We used the difference of the oxygen concentrations between the last float profile and the CTD profile at the time of float recovery to determine the drift correction for each 0.01 kg m^{-3} of potential density (σ_θ) larger than 27.5 σ_θ. The gain-corrected float oxygen data were then adjusted at each time step by applying the average drift rate to the entire profile over time. The corrected oxygen concentrations were compared with the measured values of the water samples. The differences were within the range of the nominal accuracy of the sensor (±3 μmol O_2 kg^{-1}) (Table 1).

For N + N, the sensor output values were converted to N + N concentrations following standard protocols outlined in Johnson et al. (2016). The optical wavelength offset, which accounts for the uncertainty of the wavelength registration of the diode array spectrometer, was adjusted to minimize the difference between the discrete and sensor N + N concentrations measured on the deployment cast. Corrected N + N concentrations were calculated using the new optical wavelength offset. Subsequent data quality control was implemented using the SAGE software of the Monterey Bay Aquarium and Research Institute (Maurer et al., 2021 following Johnson

Table 1
Measurement Range and Accuracy of Each Sensor

Sensor	Parameter (unit)	Range of measurement	Accuracy	Remarks
Dissolved oxygen sensor (SBE63)	Oxygen (μmol O_2 kg^{-1})	~250	±3	This accuracy is nominal. The corrected Argo data have been compared with measured oxygen value of water samples and confirmed to be within the nominal accuracy range.
DeepSUNA	Nitrate + Nitrite (μmol N kg^{-1})	~45	±2.4	This accuracy is nominal. The Argo data have been compared with nitrate and nitrite concentrations measured water samples and confirmed to be within the nominal accuracy range.
Chlorophyll fluorescence	Chlorophyll *a* (μg L^{-1})	~3	±0.1	
700-nm optical backscatter	Particulate organic carbon (μmol C kg^{-1})	~15	±0.5	

et al., 2017). The corrected N + N concentrations were compared with the measured values of water samples. The differences were within the range of the nominal accuracy of the sensor (±2.4 μmol N kg^{-1}) (Table 1).

2.3.2. Chlorophyll *a* (CHLA)

Water samples for chlorophyll *a* analysis were collected from the float deployment and recovery stations. The vertical resolution of chlorophyll *a* sampling was 25 m in the top 200 and 50 m at depths of 200–400 m. Seawater (200 mL) was poured from each Niskin bottle into an opaque bottle. Water samples were filtered through Grade GF/F Whatman 25-mm glass fiber filters (Cytiva Life Sciences, USA). The chlorophyll *a* on the filter was extracted immediately after filtration in 7 mL of N,N-Dimethylformamide in a freezer at −20°C. The extracted chlorophyll *a* was measured onboard using a fluorometer (10-AU, Turner Designs, USA). To examine the relationship between the extracted chlorophyll *a* concentrations and float fluorescence values, the float fluorescence values at the depth closest to the water sampling layers were compared with the extracted chlorophyll *a* during the time of float deployment. At the time of float recovery, the fluorescence values at the density closest to that of the layer where the water was sampled were compared to the extracted chlorophyll *a* concentration because more than one day had passed between the float observations and water sampling. The relationship between the extracted chlorophyll *a* concentrations and float fluorescence values was linear (Figure 2a). We used the empirical relationship between chlorophyll *a* concentrations and fluorescence based on data from both cruises to estimate the chlorophyll *a* concentration for each daily float profile as follows:

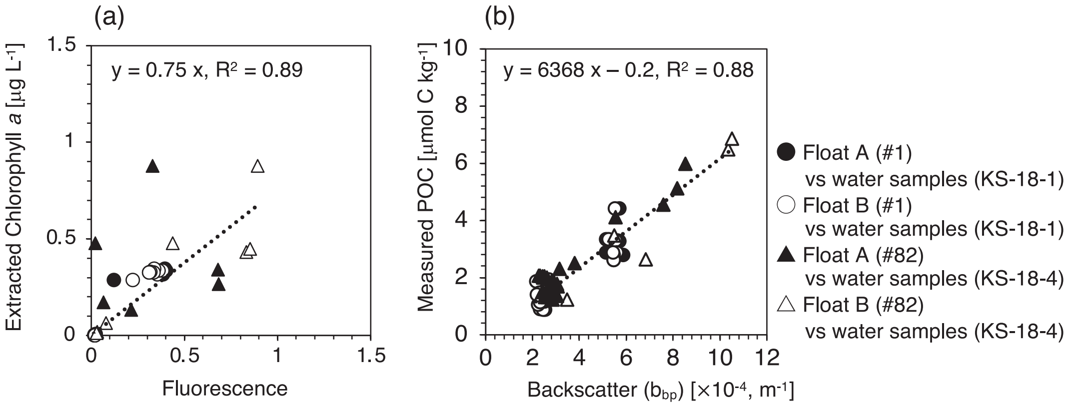

Figure 2. The relationships between (a) fluorescence measured by floats and Chl *a* concentrations from water samples and (b) backscatter (b_{bp}) measured by floats and particulate organic carbon (POC) concentrations from water samples. Solid black and open circles show fluorescence and b_{bp} measurements from the first profiles of Float A and B versus Chl *a* and POC from water samples. Solid black and open triangles show fluorescence and b_{bp} measurements from the final profile of Float A and B versus Chl *a* and POC from water samples. The black dotted lines show the linear regressions fit to the data.

$$\text{CHLA}\left(\mu\text{g L}^{-1}\right) = \text{Fluorescence value} \times 0.75, r^2 = 0.89. \tag{1}$$

The root mean squared error (RMSE) of the corrected fluorescence values versus the extracted chlorophyll *a* concentration was ±0.1 μg L^{-1} (Table 1).

We used the equation of Morel et al. (2007) to calculate the depth of the euphotic zone (Z_e) from the CHLA concentration in the shallowest layer observed by the floats. Note that the calculated Z_e (59 m for Float A and 58 m for Float B) on the first observation (January 28) was slightly shallower than the Z_e (73 m) measured by the PAR sensor attached to the CTD system during the KS-18-1 cruise. We used the Z_e estimated from the float CHLA concentration in the following discussion.

2.3.3. Particulate Organic Carbon

Water samples for POC were also collected at the float deployment and recovery stations. Seawater (5–7 L) was transferred from a Niskin bottle into a prewashed polyethylene tank through a prewashed silicon tube. Water samples ($n = 66$) were filtered through precombusted (450°C for 4 hr) Grade GF/F Whatman 47-mm glass fiber filters. The filters were stored in precombusted aluminum foil at −20°C for chemical analyses. Before analysis, samples were fumed with hydrochloric acid for 12 hr to remove particulate inorganic carbon (e.g., calcium carbonate). The acid was then removed in a vacuum desiccator, and the samples were dried in a natural convection oven at 60°C overnight (12 hr). The filters were packed in tin cups before analysis with an elemental analyzer (FLASH EA1112, Themo Fisher Scientific, USA). Alanine and glutamic acid (FUJIFILM Wako Pure Chemical Corp., Japan, Guaranteed Reagent, No. 014-01045 and 074-00505, respectively) were used as the calibration standards (0.05–0.7 mg C) and to assess analyzer stability.

The patterns of the vertical distributions of POC and backscattering (b_{bp}) were similar. There were spike-like signals in some places in the vertical b_{bp} profiles that may have reflected the presence of large particles (Bishop & Wood, 2008; Briggs et al., 2011). The relationship between POC concentrations and b_{bp} values was linear (Figure 2b). We used the empirical linear relationship between POC concentration and b_{bp} based on data from both cruises to estimate POC concentrations for each of the following daily float backscatter profiles:

$$\text{POC}\left(\text{mmol C m}^{-3}\right) = b_{bp} \times 6368 - 0.2, r^2 = 0.88 \tag{2}$$

$$\text{POC}\left(\text{mg C m}^{-3}\right) = b_{bp} \times 76416 - 2.4 \tag{3}$$

The RMSE of the POC concentrations estimated from b_{bp} values relative to measured POC concentrations was ±0.5 mmol C m^{-3} (Table 1).

The ranges of the POC concentrations and b_{bp} values in Equation 2 were 1–7 mmol C m^{-3} (15–75 mg C m^{-3}) and $2–11 \times 10^{-4}$, respectively. Cetinić et al. (2012), who made similar observations in the North Atlantic, have reported the following relationship: POC (mg C m^{-3}) = $b_{bp} \times 35{,}422\ (\pm 1{,}754)–14.4\ (\pm 5.8)$. In the Southern Ocean, Rembauville et al. (2017) and Schallenberg et al. (2019) have reported that POC (mmol C m^{-3}) = $b_{bp} \times 3963.45 - 0.6$ and POC (mg C m^{-3}) = $b_{bp} \times 37{,}601 - 4.95$, respectively. The differences maybe attributable to differences between regions. The previous studies were conducted in subarctic and polar regions, where POC concentrations are high in the surface layer, and large phytoplankton (i.e., diatoms) are dominant. In contrast, this study was conducted in a relatively oligotrophic subtropical region where POC concentrations have been reported to be low (Mino et al., 2023) even in the surface layer, and the phytoplankton are small (Fujiki et al., 2016). Small particles are known to be associated with low b_{bp} indices (Morel & Ahn, 1991) and therefore tend to yield higher coefficients in the POC–b_{bp} relationship.

2.4. Satellite and Reanalysis Data Sets

We used 1/4° × 1/4° daily gridded absolute dynamic topography (ADT) from the Archiving, Validation, and Interpretation of Satellite Oceanographic (AVISO) data set (Ducet et al., 2000) from the *Centre national d'études spatiales*. We downloaded the 1-km horizontal resolution surface chlorophyll *a* concentrations from the Moderate Resolution Imaging Spectroradiometer-Aqua (MODIS) satellite level 2 local area coverage website (https://oceancolor.gsfc.nasa.gov/cgi/browse.pl) from 15 March (A2018074031000.L2_LAC_OC.nc), 25 March

(A2018084034500.L2_LAC_OC.nc), and 29 March (A2018088032000.L2_LAC_OC.nc) of 2018. We used the daily microwave optimally interpolated sea surface temperature (SST) data with 8-km horizontal resolution produced by Remote Sensing Systems (https://data.remss.com/SST/daily/mw_ir/v05.1/netcdf/2018/). We used the ERA5 hourly reanalysis data (1/4° horizontal resolution) from the European Centre for Medium-Range Weather Forecasts (https://www.ecmwf.int/en/forecasts/datasets/reanalysis-datasets/era5) for surface heat fluxes and wind stresses during the observation period.

2.5. Omega Equation

To diagnose whether the front was undergoing frontogenesis or frontolysis, we calculated the frontogenesis function, $\boldsymbol{Q} \cdot \nabla_h b / |\nabla_h b|$, where Q is the Q vector (Equation 4), b is buoyancy, and ∇_h is the horizontal gradient operator. Ignoring advection by vertical flow and friction, the $\boldsymbol{Q} \cdot \nabla_h b / |\nabla_h b|$ equals the material derivative of buoyancy horizontal gradient $\frac{D_q |\nabla_h b|}{D_q t}$, where $\frac{D_q}{D_q t} = \frac{\partial}{\partial t} + u \frac{\partial}{\partial x} + v \frac{\partial}{\partial y}$, with negative and positive values indicating respective frontolysis and frontogenesis, respectively. In addition, the horizontal divergence of the Q vector, $\nabla_h \cdot \boldsymbol{Q}$, is used to diagnose the sign of the vertical flow. When $\nabla_h \cdot \boldsymbol{Q} > 0$ there is downwelling motion and $\nabla_h \cdot \boldsymbol{Q} < 0$ upwelling motion (Gill, 1982; Hoskins & Pedder, 1980). The Q vector (e.g., Hoskins et al., 1978), which is proportional to the rate of change in velocity along isopycnal as well as the rate of change in buoyancy gradients following the horizontal flow, is defined as

$$\boldsymbol{Q} = (Q_1, Q_2) = \left(-\frac{\partial u}{\partial x}\frac{\partial b}{\partial x} - \frac{\partial v}{\partial x}\frac{\partial b}{\partial y}, -\frac{\partial u}{\partial y}\frac{\partial b}{\partial x} - \frac{\partial v}{\partial y}\frac{\partial b}{\partial y} \right). \tag{4}$$

We calculated $\boldsymbol{Q}$ and $\boldsymbol{Q} \cdot \nabla_h b / |\nabla_h b|$ using the daily mean horizontal velocity and density available from global eddy-resolving ocean reanalysis data (1/12° horizontal resolution, Global_ReAnalysis_phy_001_030; provided by the Copernicus Marine Environment Monitoring Service; http://marine.copernicus.eu), which do not include vertical velocity fields.

3. Results

3.1. Float Observations During February

Wind stresses were higher in early February but declined from roughly 18 to 26 February (Figure 3a). Hourly averaged heat fluxes of the surface layer were negative for most of the day, and the daily averaged fluxes were always negative (Figure 3b). The temporal variation of the heat flux was a mirror image of the wind stress. The Z_m (the average depth during the period was 160 m) often greatly exceeded the Z_e (the average for the period was 52 m) (Figure 3c). However, Z_m equaled or was shallower than Z_e for a few days when the wind stress weakened (e.g., 3–4 and 19–23 February). The water temperature from the surface to a depth of 200 m exceeded 18°C and increased slightly with time (Figures 4a and 4b). The salinity was mostly above 34.85 from the surface to a depth of 200 m (Figures 4c and 4d). For most of February, the floats probably observed subtropical water with a salinity less than 38.5 (hereafter STW, e.g. Sukigara et al., 2014) east of the Kuroshio and south of the Kuroshio Extension (Figures 5a and 6a). However, the distribution of SST on 22 February (Figure 6b) indicated that warm water influenced by the Kuroshio with a salinity greater than 38.5 (hereafter KSTW) extended into the vicinity of the float and affected the observations of the floats (Figure 5a).

Temporal variations of DO profiles (Figures 4g and 4h) were similar to the variations of water temperature and salinity (Figures 4a–4d); DO concentrations were homogeneous and high within the mixed layer and decreased with depth from the depth of the thermocline. The percentages of oxygen saturation were slightly below 100% in the surface mixed layer and underwent temporal variations similar to those of DO (Figures 4i and 4j). Unlike DO, N + N concentrations were low in the mixed layer (1–2 μmol N kg^{-1}) and increased with depth below about 200 m (>2 μmol N kg^{-1}, Figures 4k and 4l). This pattern was likely due to nutrient uptake by phytoplankton within the euphotic zone and surface mixing processes. The distributions of the concentrations of CHLA (Figures 4m and 4n) and POC (Figures 4o and 4p) were similar to the distribution of DO, that is, higher in the surface mixed layer and decreased with depth. Slight increases of the surface CHLA concentrations were observed during interludes of weak wind stress on 3 and 4 February and after 19 February in the case of Float A and during 9–11 February and after 19 February in the case of Float B. However, these increases were small both

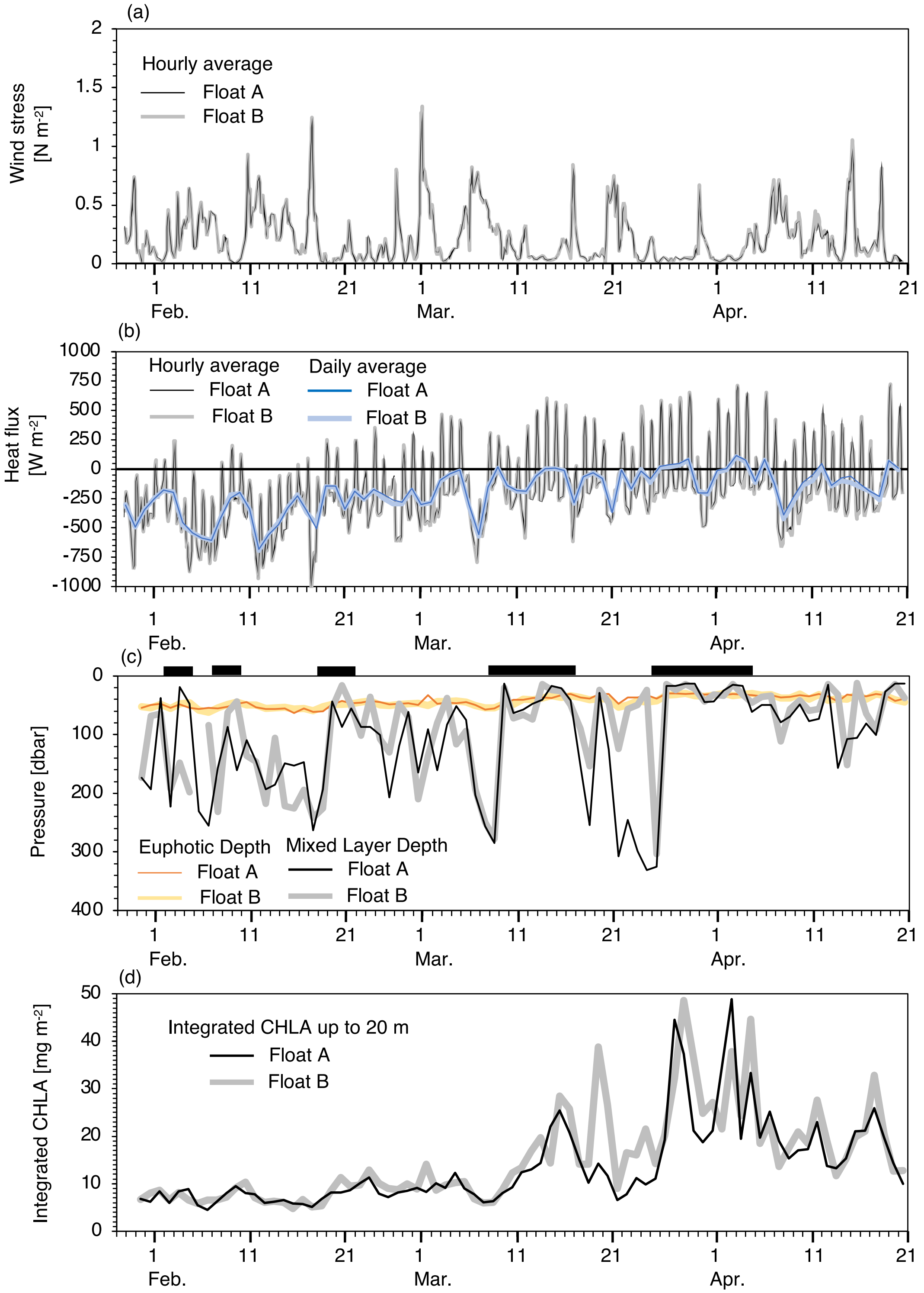

Figure 3. (a) Change of hourly wind stresses at the position of Float A (black thin line) and B (gray thick line), respectively. (b) Change of heat flux at the hourly position of Float A (black thin line) and B (gray thick line), and at daily position of Float A (blue thin line) and B (pale blue thick line). (c) Temporal variations of the mixed layer depth and the depth of the euphotic zone observed by Float A (black thin line for the mixed layer depth and red thin line for the depth of the euphotic zone) and B (the gray thick line for mixed layer depth and the yellow thick line for depth of the euphotic zone). The black lines at the top of the graph indicate when the CHLA concentration in the surface layer increased after deep mixing. (d) Temporal variations of integrated CHLA over the top 20 m observed by Float A (black thin line) and Float B (gray thick line).

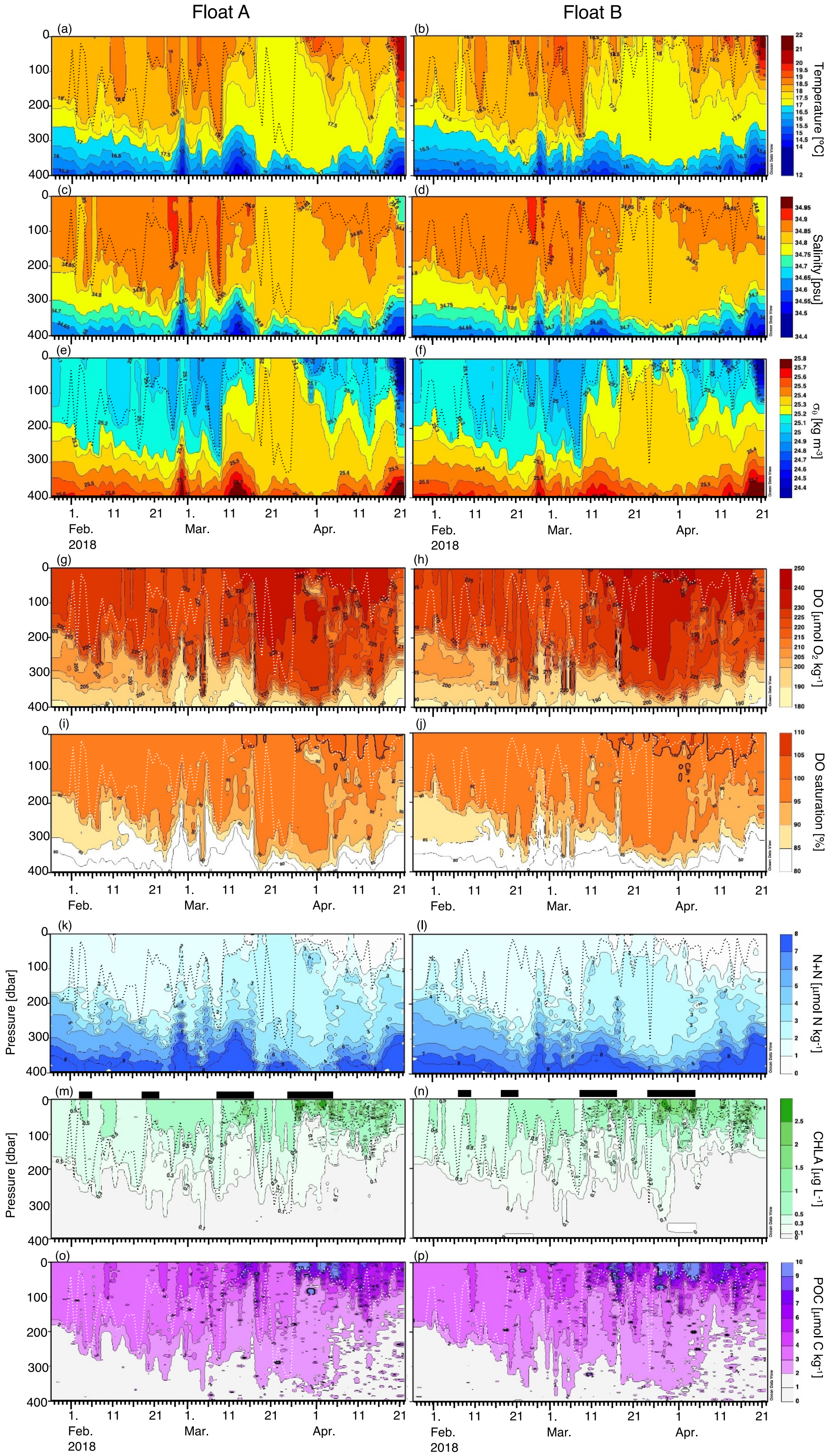

Figure 4. Time series of vertical profiles of (a and b) temperature, (c and d) salinity, (e and f) potential density (s_{q}), (g and h) oxygen concentrations (dissolved oxygen (DO)), (i and j) DO saturation, (k and l) nitrate plus nitrite concentrations (N + N), (m and n) chlorophyll *a* concentrations (CHLA), and (o and p) particulate organic carbon concentrations (POC) observed by Float A and B. Bold black lines in panels (a–f) and (k–n) and bold white lines in panels (g–j) and (o, p) indicate the depth of the mixed layer. The black lines at the top of Figures 4m and 4n indicate the periods of increased CHLA after deep mixing.

at the surface (Figure 3d) and in the water column (Figure S1 in Supporting Information S1) throughout the observation period, and concurrent increases of POC and N + N were barely apparent.

3.2. Float Observations During March

Intense wind stress was observed during the first eight days of March and during 20–23 March (Figure 3a). Daily averaged heat fluxes during March were often negative (Figure 3b). Nevertheless, the monthly mean heat fluxes indicated weaker surface cooling during March (-109 W m^{-2}) than February (-335 W m^{-2}). The Z_m when the wind stress was large tended to be much deeper than the Z_e (Figure 3c). The depths of the mixed layer on 8 March (>280 m) and 25 March (>300 m) were the deepest throughout the study period at both floats. The Z_m rapidly shoaled (<20 m) on the days after this deep mixing (9 and 26 March). In contrast to February, these shallow mixed layers were observed continuously for more than a week after the deep mixing. The floats recorded large variations of temperature and salinity on each isopycnal line (Figure 5b) between the STW and KSTW (Figure 6c). On 14 March, the floats changed direction and gradually moved northward into the Kuroshio (Figure 1). The floats then recorded water with characteristics similar to those of the KSTW (Figure 5c).

When the mixed layer deepened (6–8 and 18–25 March), the concentrations of DO were homogeneous within the mixed layer (Figures 4g and 4h). When the mixed layer shoaled, DO increased near the surface because the periods between storms were longer. Supersaturation of oxygen, which was not apparent during February, was often observed in the surface layer (Figures 4i and 4j). High concentrations of CHLA (>1.5 μg L^{-1}, Figures 4m and 4n) and POC (>8 μmol C kg^{-1}, Figures 4o and 4p) and low concentrations of N + N (<1.0 μmol N kg^{-1}, Figures 4k and 4l) were apparent in the same layer and at the same time when the DO was supersaturating. The increase of CHLA in late March was the largest and continued for the longest period of time (26 March–5 April) during this study.

3.3. Float Observations During April

Wind stresses were still high on many days during April (Figure 3a). Heat fluxes changed in response to wind stress (Figure 3b). The maximum Z_m during April—about 155 m in mid-April—was shallower than during the other months (Figure 3c). The time series of vertical profiles of temperature revealed that temperatures were sometimes higher in the surface layer (Figures 4a and 4b). This pattern was more pronounced at Float B, which was closer to the Kuroshio Current (Figure 6d). Water temperatures and salinities during April were mostly similar to those of the KSTW (Figure 5d). At the end of the observations (19–20 April), high water temperatures (>20°C), low salinities (<34.8), and low densities (<24.5 kg m^{-3}) were observed between the surface and a depth of 50 m (Figures 4a–4f). That water was likely Kuroshio water influenced by coastal water.

Before 5 April, high DO concentrations and oxygen saturation were observed within the euphotic zone (Figures 4g–4j), where the CHLA (Figures 4m and 4n) and POC (Figures 4o and 4p) concentrations were high, and that of N + N was low (Figures 4k and 4l). After 5 April, higher DO, oxygen saturation, CHLA, and POC and low N + N were observed within the euphotic zone, but low oxygen saturation (less than 95%), low CHLA (less than 0.1 μg L^{-1}), low POC (less than 2 μmol C kg^{-1}), and higher N + N (>3 μmol N kg^{-1}) were apparent at depths greater than 100 m. Nagai and Clayton (2017) have reported that isopycnals shoal and nitrate concentrations on isopycnals in the subsurface (depths of ~100 m) become higher toward the Kuroshio axis. Those vertical distributions of DO, CHLA, POC, and N + N is probably specific to the Kuroshio Current.

4. Discussion

4.1. Intermittent Chlorophyll Increases After Deep Mixing

During the spring transition season in the subtropical ocean, phytoplankton blooms are assumed to be caused by the simultaneous improvement of nutrient and light conditions due to deep convective mixing by cooling during the winter and subsequent stratification of the surface layer by warming during the spring, respectively. This vertical one-dimensional (1-D) physical-biogeochemical explanation has been described as the critical depth hypothesis (Sverdrup, 1953).

In February, temperature and density profiles after deep mixing (Figures S2a–S2l in Supporting Information S1) revealed large changes accompanied by increases of CHLA, even though the daily averaged heat flux indicated strong surface cooling. The implication was that the restratification could not be explained solely by a vertical 1-D

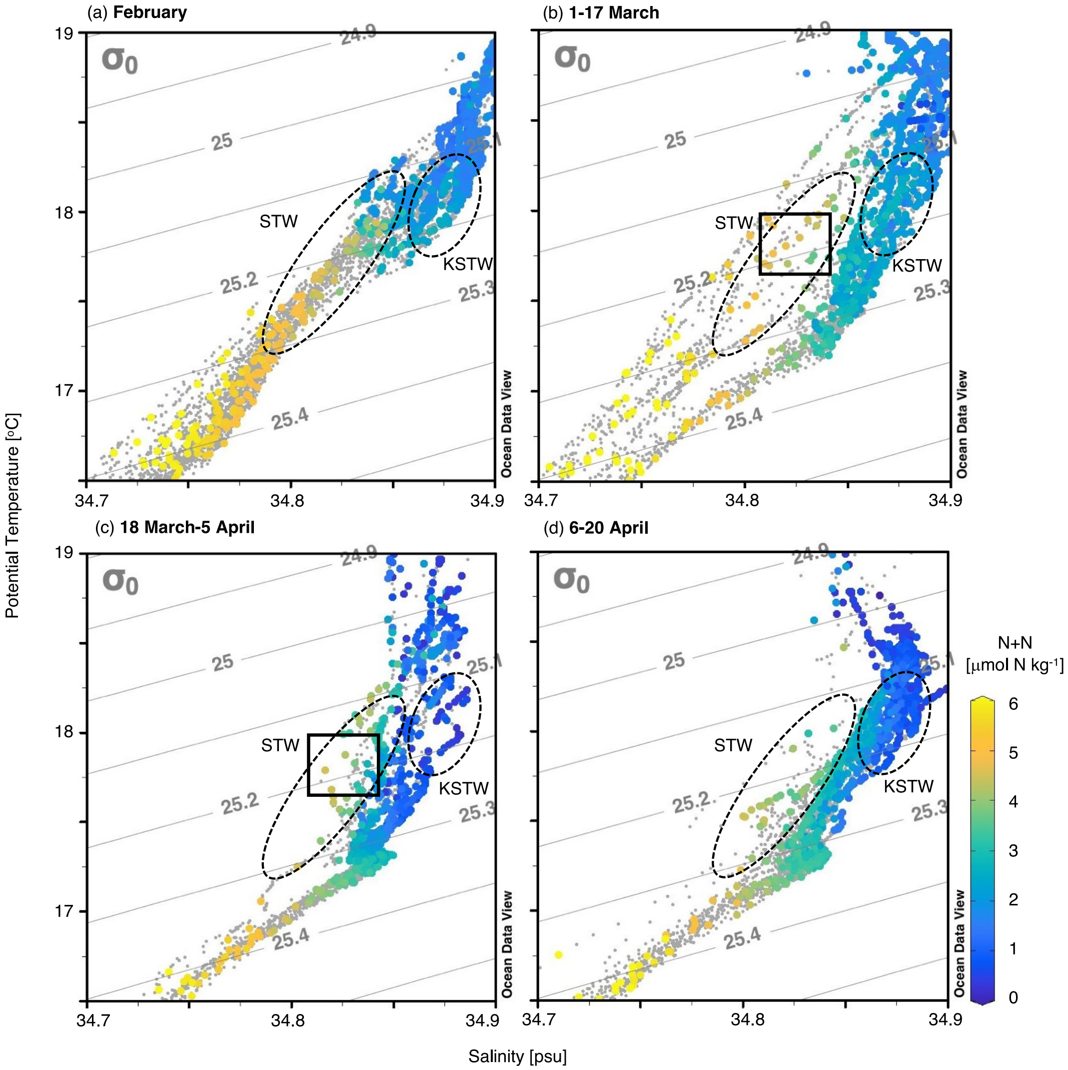

Figure 5. Temperature-salinity diagram for each period (a–d). Colored dots indicate N + N concentrations. Gray dots indicate values without N + N data. The dashed ellipses show the characteristic temperature-salinity distributions of STW (the subtropical water) and KSTW (the subtropical water influenced by the Kuroshio Current water). The black boxes in panels (b and c) show the area bounded by potential temperatures of 17.7–18°C and salinities of 34.81–34.84.

process. The floats in fact observed a variety of water mases. However, the small changes of water temperature and density in the euphotic zone recorded by Float A on 2–4 February indicated that the float observed biological processes in the same water, but the increase of CHLA was small, less than 0.5 μg L^{-1} (Figures 4m and 4n, Figure S2a–S2c in Supporting Information S1). There was little increase of the integrated CHLA in the surface layer (0–20 m) and the upper 400 m (Figure 3d and Figure S1 in Supporting Information S1), respectively. The numerical simulation by Taylor and Ferrari (2011) indicated that it took several days after mixing for turbulence to weaken and phytoplankton to increase. The short duration between atmospheric events (Figures 3a–3c) may therefore have prevented the postmixing CHLA concentration from increasing in our study area.

The mixed layer was shallower than 100 m for more than 5 days in the float observation area during March (Figure 3c). The wide variation of the water temperature and density profiles during 8–15 March indicated that the floats were observing a variety of waters between STW and KSTW (Figure 5b and Figure S2m–S2r in Supporting Information S1). Although we could not regard the changes of the biogeochemical parameters (DO, CHLA, N + N, and POC) in the surface (0–50 m) layer (Figure 4) as the result of a vertical 1-D process, those changes indicated that there was more active phytoplankton production during the longer restratification period than during February. During the mixing-restratification period from 25 March to 5 April, the floats observed waters similar to KSTW

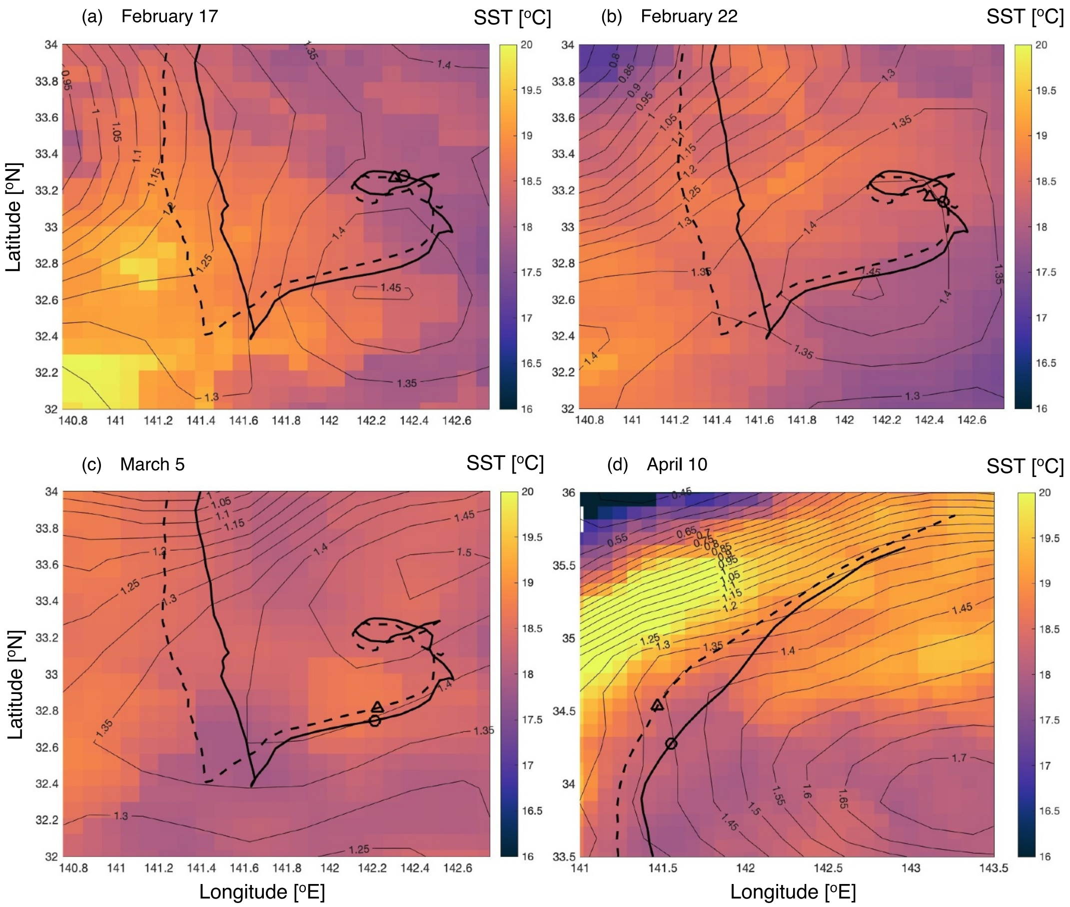

Figure 6. Satellite images of sea surface temperature (SST, colors) and absolute dynamic topography (ADT, contours) around the floats on 17 February (a), 22 February (b), 5 March (c), and 10 April (d). Float positions indicated by circles for Float A and triangles for Float B. Black solid and dashed lines in panels show the trajectory of Float A and B.

(Figure 5c), but the surface (0–100 m) water temperature and salinity changed greatly (Figure S2s–S2x in Supporting Information S1). The CHLA concentrations in the euphotic zone also increased rapidly after the restratification (Figures 3d, 4m, and 4n), which occurred much more rapidly than the biological responses (several days). The implication was that the phytoplankton increased before the turbulence weakened (Chiswell, 2011). The integrated CHLA in the surface layer (0–20 m) and the water column (0–400 m) were larger than at any other time during the observation period (Figure 3d and Figure S1 in Supporting Information S1), and the surface concentrations (>1.5 μg L^{-1}) were comparable to the concentrations associated with the spring bloom in this region (Matsumoto et al., 2021). We will discuss the mechanism responsible for this phenomenon in Section 4.2.

From 1 to 5 April, concentrations of CHLA and POC were high in the euphotic zone (Figures 4m–4p). The subsequent decrease of CHLA in the euphotic zone (Figure 3d) was accompanied by low N + N (<1 μmol N kg^{-1}). The mixed layer was deep (~150 m) on 13 and 14 April, but the N + N never exceeded 1 μmol N kg^{-1}. If allochthonous nutrients were not supplied, then concentrations of CHLA would gradually decrease near the sea surface, and a subsurface chlorophyll maximum (Cullen, 1982), which was not apparent from our observations, would be formed by the relatively shallow nitracline.

4.2. Vertical Variations of Biogeochemistry Due to Complex Structure of the Water Column in Late March

4.2.1. Enhancement of Surface Productivity

After formation of the deep mixed layer in late March (25 March), the surface layer rapidly restratified (Figure 3c), possibly because of a combination of local surface heating and lateral advection of warm water.

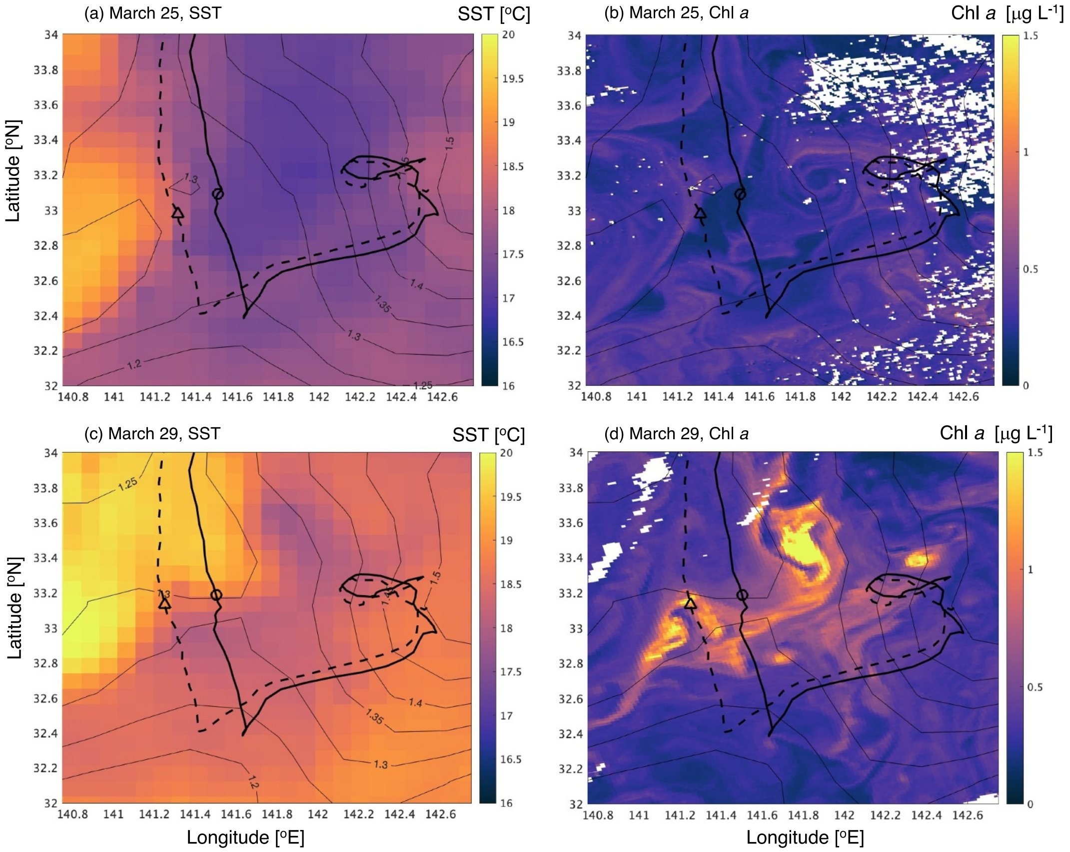

Figure 7. Satellite images of sea surface temperature (SST; a and c) and Chl *a* (b and d) around the floats on 25 March (a and b) and 29 March (c and d). The contours in each figure show absolute dynamic topography. Float positions are indicated by a circle for float A and a triangle for float B. Black solid and dashed lines in panels show the trajectory of Float A and B.

Satellite SST images indicated that the temperature around the floats on 29 March (Figure 7c) could have been affected by warm water from the west that presumably originated from the Kuroshio Current. Satellite chlorophyll concentrations increased in fronts between the warm and colder water on 29 March (Figures 7c and 7d).

We estimated that the daily rate of increase of POC in the upper 20 m of the water column during this period (25–29 March) was estimated to have been 570 mg C m^{-2} d^{-1} at Float A (Figure 8d) and 384 mg C m^{-2} d^{-1} at Float B (Figure 8j). Those increases were comparable to those reported by Matsumoto et al. (2016) at nearby time series station S1 (30°N, 145°E), where net primary productivity integrated throughout the euphotic zone was 296–849 mg C m^{-2} d^{-1} during February and April 2011, and the annual average was 369 mg C m^{-2} d^{-1}. Sasai et al. (2016) have reported that primary productivity during January–March, estimated from satellite (MODIS) chlorophyll data using the vertical generalized production model (VGPM, Behrenfeld & Falkowski, 1997), was 400–800 mg C m^{-2} d^{-1}, and the highest rates were in March and April. Although the accuracy of our POC-based estimations of productivity was diminished by the quasi-Lagrangian nature of the float observations, our results, which suggested that productivity was higher within the study area, were consistent with the results of previous studies (Matsumoto et al., 2016; Sasai et al., 2016).

Examination of the relationship between temperature and N + N (POC) averaged within the upper 20 m of the water column during 25–31 March revealed that the higher the temperature of the water, the lower (higher) the concentration of N + N (POC) (Figures 9b and 9c). These results suggested that phytoplankton in the surface layer took up nutrients and produced POC via photosynthesis rapidly and efficiently. However, the molar ratio of the decrease of N + N to the increase of POC was about 4.5, which was lower than the range of variation (6–9, Xiao et al., 2021) of the stoichiometric ratio of marine phytoplankton (Redfield ratio, Redfield et al., 1963). This discrepancy was perhaps due to differences between the methods used to estimate the C/N ratio. Some of the particulate organic matter produced in the ocean surface layer is removed from the surface to the deeper layer by

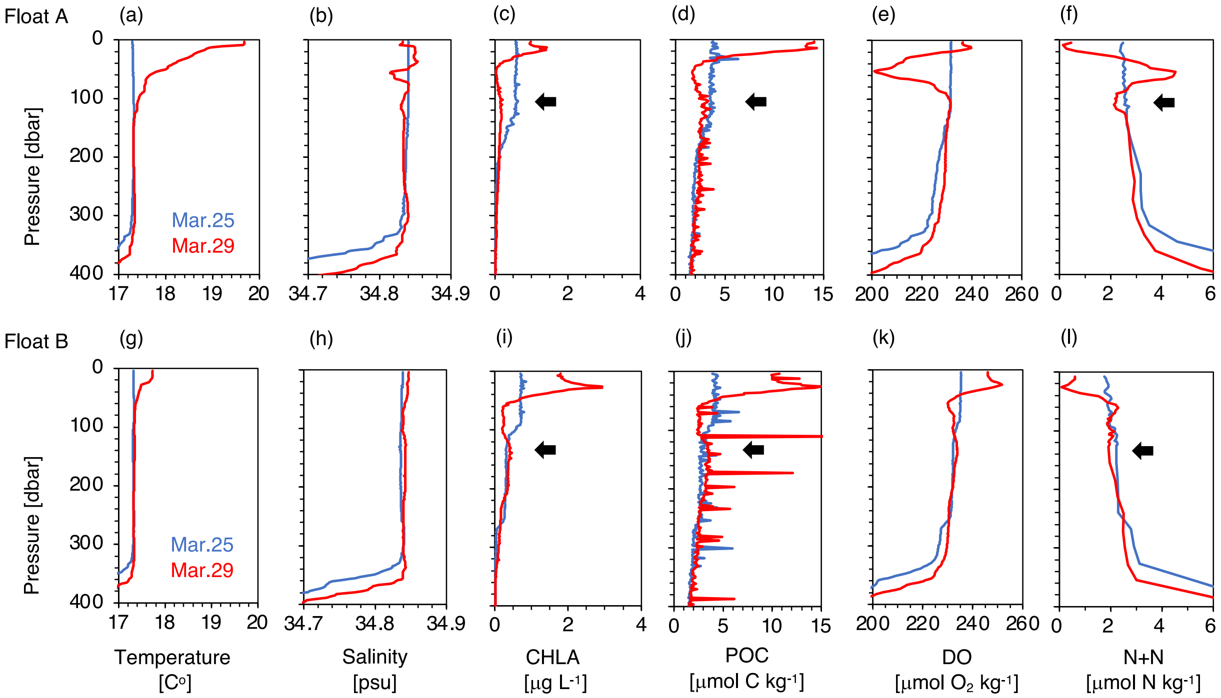

Figure 8. Vertical profiles of (a and g) temperature, (b and h) salinity, (c and i) CHLA, (d and j) particulate organic carbon, (e and k) dissolved oxygen, and (f, l) N + N on 25 March (blue) and 29 March (red) for Float A (top row) and B (bottom row). Black arrows in panels (c, d, f, i, j, and l) indicate downwelling of the surface water due to secondary circulation.

settling. The increases of POC determined in this study could therefore have been underestimated. The trend of POC was not reflected by a similar trend of CHLA (Figure 9a). The reason for this discrepancy maybe that the response of the phytoplankton to an increase of irradiance in the stratified surface layer was to decrease their intracellular chlorophyll concentration (i.e., thereby reducing their light-harvesting capacity) to avoid photooxidative damage (Behrenfeld et al., 2015; Graff & Behrenfeld, 2018; Taylor et al., 1997). The relationship between temperature and the POC/CHLA ratio in the surface layer (Figure 9d) indicates that the phytoplankton that remained in the warmer (less dense) water had acclimated to the high-light environment for a longer period. Another process that would increase the POC/CHLA ratio would be the loss of pigments from phytoplankton and their conversion to detritus as they die (Geider, 1987). Our results could not distinguish between acclimation and death of phytoplankton. However, the high POC concentrations near the surface indicate that active photosynthetic production of particulate organic matter had occurred recently.

A comparison of these average concentrations of CHLA, N + N, and POC in the upper 20 m of the water column with the corresponding concentrations measured during other periods revealed that the POC concentrations at the end of March were higher at most water temperatures (Figure 9c). From February to mid-March, N + N concentrations were high (Figure 9b), but CHLA and POC concentrations were low (Figures 9a and 9c), possibly because frequent deepening of the mixed layer could have limited the growth of phytoplankton, as described in Section 4.1. During April, however, Float B recorded low N + N concentrations (<0.5 μmol N kg^{-1}) that were similar to those observed at the end of March near the Kuroshio Current. At the same time, however, the POC concentrations were lower during April than at the end of March. These results suggested that particulate organic matter produced by the uptake of nutrients was removed from the surface layer by settlement, and nutrient-poor water remained in the surface layer during April.

4.2.2. Low DO and High N + N Water in the Subsurface Layer

Low concentrations of DO (Figures 8e and 8k), CHLA (Figures 8c and 8i), and POC (Figures 8d and 8j) and high concentrations of N + N (Figures 8f and 8l) were recorded at a depth of ~50 m on 29 March, especially by Float A. The temperature at a depth of ~50 m on 29 March was higher (17.7–18°C) than the temperature (17.3°C) before water column restratification (25 March, Figure 8a). Similar temperatures (17.7–18.0°C) and salinities

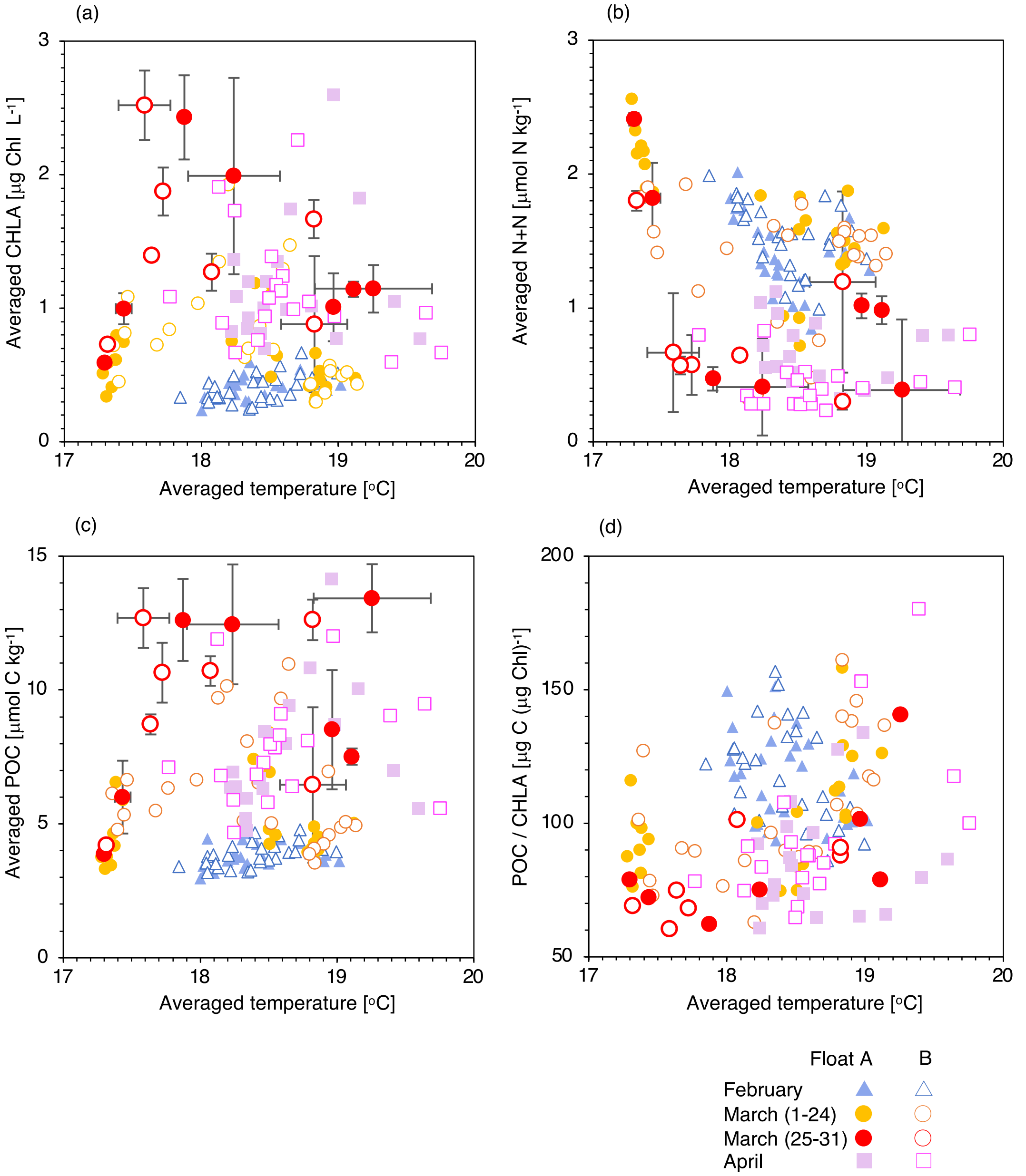

Figure 9. Relationship of (a) averaged CHLA, (b) averaged N + N, (c) averaged POC, and (d) POC/CHLA ratio for averaged temperature between the surface and a depth of 20 m on each day. The whiskers from each red point in panels (a–c) indicate standard deviations.

(34.81–34.84) as well as N + N concentrations were observed in early March (black box in Figures 5b and 5c). In profiles of DO versus density, water with a DO of 200 μmol kg^{-1} in the density range 25.10–25.20 σ_θ on 29 March was also observed in early March (blue dots in Figure 10a). Those observations led us to conclude that subsurface water on 29 March was likely upwelled from depths of 200–300 m (Figure 10b) to depths of 50–100 m rather than advected into the euphotic zone from another area. The mechanism responsible for this upwelling is explained in Section 4.2.3. We further note that the N + N profile of Float A indicated that the N + N concentration was higher in the upwelled water observed on 29 March than in the mixed layer on 25 March (Figure 8f). Upwelled water with a high N + N concentration was also found in other profiles (30–31 March and 1 April for Float A and 2 April for Float B). The N + N concentration in the water upwelled from depths of 50–100 m was 1.4 times the N + N concentration of water at depths of 100–150 m (Figure 11).

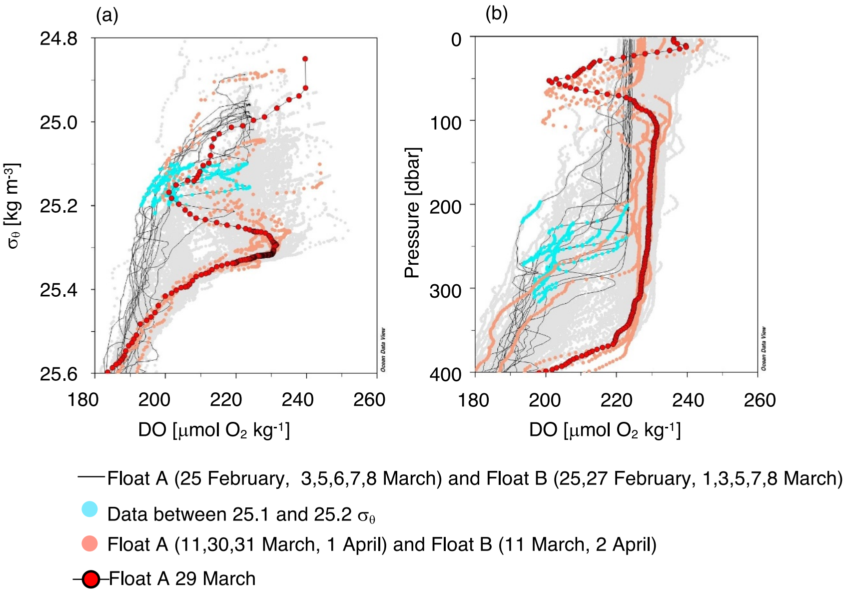

Figure 10. Vertical profiles of (a) dissolved oxygen (DO) versus potential density (s_q) and (b) DO versus pressure. Black solid lines indicate profiles with DO values near 200 mmol O_2 kg^{-1} between 25.1 and 25.2 σ_θ in late February and early March. Pale blue dots indicate data between 25.1 and 25.2 σ_θ in late February and early March. Magenta dots indicate profiles with low DO (about 200 mmol O_2 kg^{-1}) in the surface 100 m in March. Red dots surrounded by black lines indicate the profile on 29 March, which are strongly indicative of a multilayer structure of the water column.

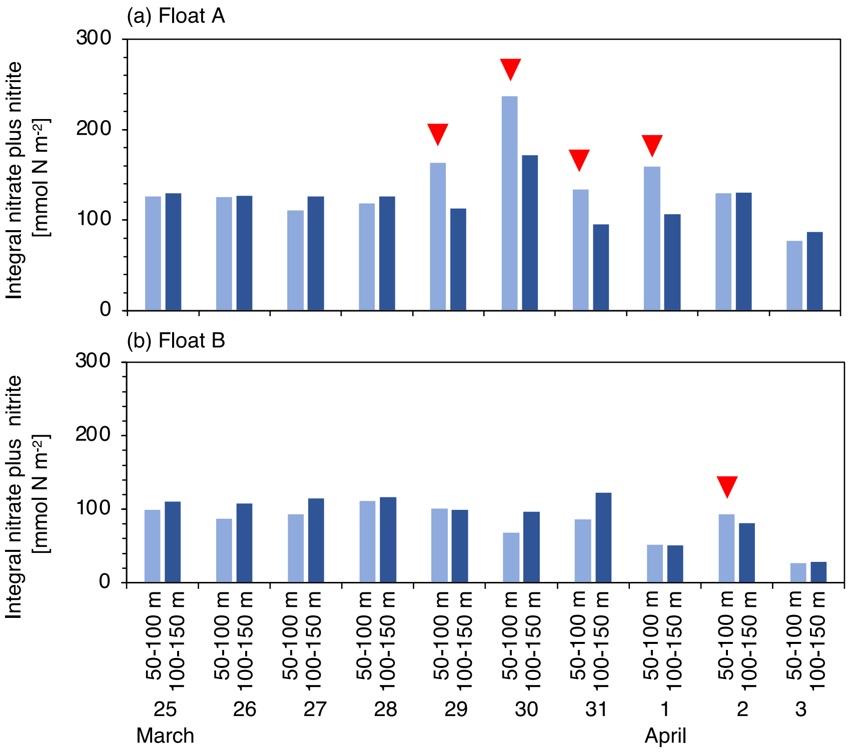

Figure 11. Temporal variation of integrated N + N values between 50 and 100 m (pale blue bars) and 100–150 m (dark blue bars) for Float A (a) and Float B (b). The red inverted triangles in the figure indicate when the value between 50 and 100 m was higher than the value between 100 and 150 m.

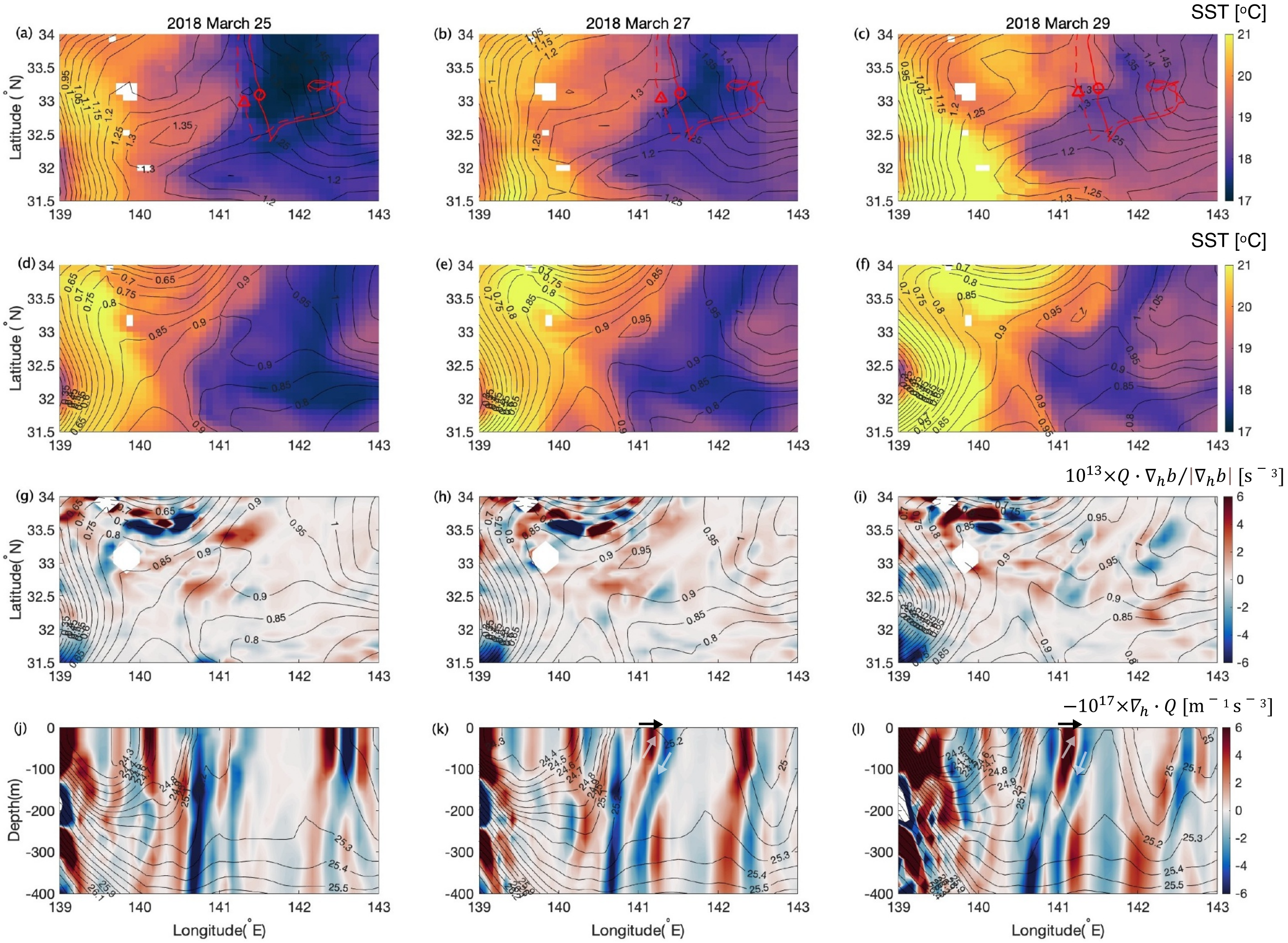

Figure 12. Satellite images of sea surface temperature (SST) (colors) and absolute dynamic topography (contours) on (a) 25, (b) 27, and (c) 29 March. Float positions indicated by circles for Float A and triangles for Float B. Black solid and dashed lines show the trajectory of Float A and B. Horizontal distribution of SST (colors) and sea surface height (SSH) (contours) from the ocean reanalysis outputs on (d) 25, (e) 27, and (f) 29 March. Horizontal distribution of $10^{13} \times Q \cdot \nabla_h b/|\nabla_h b|$ (colors) at a depth of 186 m and SSH (contours) on (g) 25, (h) 27, and (i) 29 March. Vertical cross-section of $-10^{17} \times \nabla_h \cdot Q$ (colors) and density (contours) across 32.5°N on (j) 25, (k) 27, and (l) 29 March. Black and white arrows in panels (k and l) indicate water movements.

4.2.3. Mechanism of Formation of Multilayer Vertical Structure of the Water Column

Mesoscale strain causes a frontogenesis and generates an ageostrophic secondary circulation (Lapeyre & Klein, 2006; Legal et al., 2007). In late March, the temporal variations of ADT and SST indicated that a meander of the Kuroshio Current had pushed warm water toward the floats from both west and east and had formed a thermal front (Figures 12a–12c). We used reanalysis data to diagnose the secondary circulation that resulted from these frontal features (Figures 12d–12f). The horizontal distributions of the frontogenesis function $Q \cdot \nabla_h b/|\nabla_h b|$ at a depth of 186 m (Figures 12g–12i) became positive at the front around 141°E (e.g., 32.5°N). The indication was that a front had formed during this period. During the frontogenesis, ageostrophic motions caused a flattening of isopycnal surfaces that created an overturning cell in the across-front direction (e.g., McKee et al., 2023). The overturning cell included an upward flow at the low-density side and a downward flow at the high-density side (see white arrows in Figures 12k and 12l, and red broken arrows 2 and 3 in Figure 13b), flattening the front as opposed to the confluence flow at the surface (see black arrows at the top of abscissa in Figures 12k and 12l, and the red broken arrow 1 in Figure 13b). This overturning could explain the observed float profiles of biogeochemical metrics. Because density surfaces near fronts are tilted, ageostrophic secondary circulation could explain the observed biogeochemical vertical profiles, as described below. Submesoscale ageostrophic dynamics such as mixed layer eddies (Fox-Kemper et al., 2008; McKee et al., 2023) may have further enhanced restratification and vertical motions near the sea surface. These submesoscale features were confirmed as submesoscale

(a) Water structure during the vertical mixing

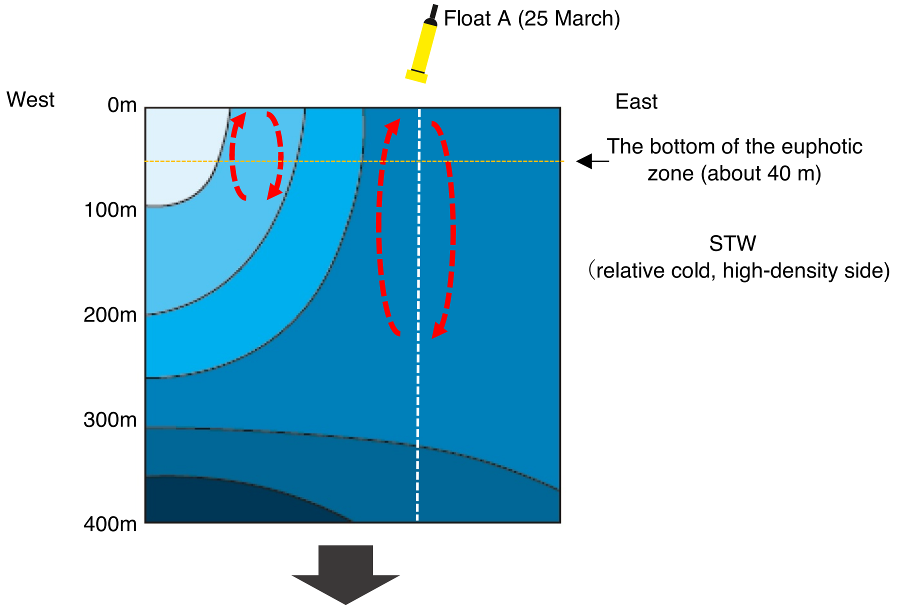

(b) Water structure after the mixing in late March

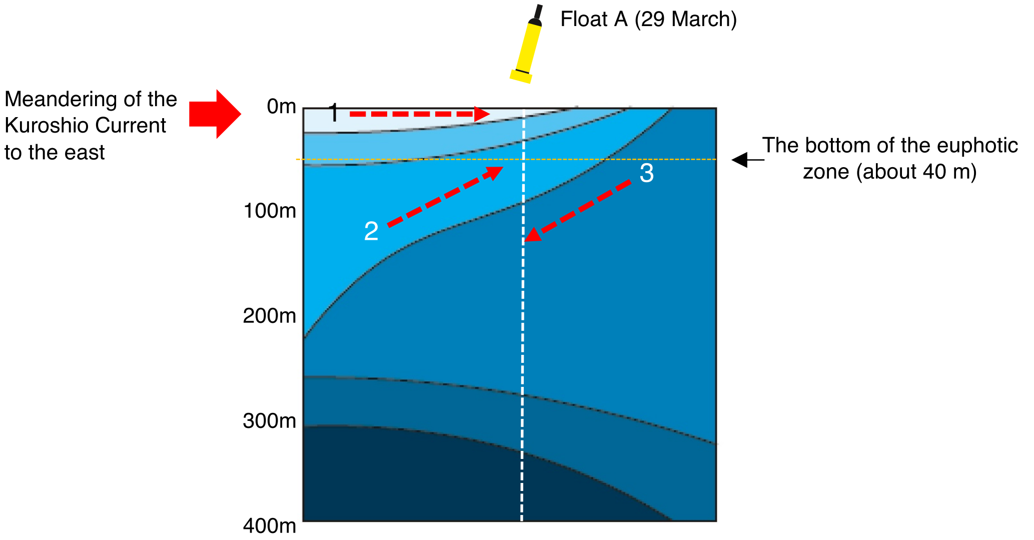

Figure 13. Schematic diagram illustrating the process of multilayer structure formation. (a) East-west cross-section near the float during the days of mixing in 20–25 March. (b) East-west cross-section near the float during the days of restratification during 26–29 March. The blue gradient colors in the figure indicate densities. Red arrows in panel (a) indicate water movements by mixing; those in panel (b) indicate water movements (cell overturn) by secondary circulation. The movements of each water in panel (b) are explained as follows: (1) Lower-density water mixed by the storm extended to the surface and lay above high-density water. Phytoplankton increased rapidly in the shallow, well-lit layer (0–20 m) and consumed nutrients in that layer. (2) The extension of surface water entrained subsurface (100–200 m) water with higher nutrient concentrations and transported it into the lower part of (or just below) the euphotic zone (~50 m). On 29 March, nutrients had just been transported, and few nutrients had yet been used by phytoplankton. (3) The surface water in the high-density side was subducted to the subsurface (~100 m). During this time, phytoplankton in this water were entrained into the subsurface layer.

cyclonic eddies, and high CHLA concentrations were clearly apparent in the satellite images after the formation of a deep mixed layer (Figures 7b and 7d). However, we could diagnose only vertical motions associated with the mesoscale features because of the limited spatial resolution of the ocean reanalysis data.

A storm during 21–25 March (Figure 3a) deepened the mixed layer (Figure 3c) and entrainment of nutrients from deeper layers (Figures 4k and 4l). Warm water subsequently overlaid the cold water (Figures 8a and 8g), and the flux of light needed for phytoplankton photosynthesis in the surface layer (0–20 m) increased. These changes could explain the rapid growth of phytoplankton (Figures 7b, 7d and 8c and 8i) during the restratification period. The low concentrations of CHLA, POC, and DO (Figures 8c–8k) and high concentrations of N + N (Figures 8f and 8l) at depths of 20–100 m on 29 March indicated that the water had come directly from greater depths. This conclusion was consistent with the pattern of secondary circulation around the front (∼141°E in Figures 12k and 12l). The upwelled water from the twilight layer supplied higher concentrations of nutrients than did vertical mixing to the lower part of the euphotic zone (20–50 m) or just beneath it (50–100 m) (Figures 8f, 8l and 11).

The spatial distribution of vertical velocities also indicated downwelling due to secondary circulation (Figures 12j–12l). That downwelling could have created the small peak of CHLA (Figures 8c and 8i) and POC (Figures 8d and 8j) and slight decrease of N + N (Figures 8f and 8l) at depths of 100–200 m. This scenario is similar to the effect of the mixed layer pump in the eutrophic subarctic ocean (Boyd et al., 2019; Dall'Olmo et al., 2016; Lacour et al., 2019; Omand et al., 2015), where particles are transported into the twilight layer. In the oligotrophic subtropics (this study), we observed that secondary circulation led to a rapid increase of phytoplankton in the upper euphotic zone and supplied high concentrations of nutrients to the lower euphotic zone or to water just below the euphotic zone.

5. Conclusions

We combined data from satellites and two biogeochemical (BGC)-Argo floats in this study to analyze how changes of water properties during the spring transition (from January to April 2018) influenced biological activity in the subtropical western North Pacific Ocean. The study area was delineated by the meandering Kuroshio main current, the Kuroshio Extension, and eddies composed of water with different characteristics. The floats were equipped with several BGC sensors and were programmed to profile daily in order to capture spatial and temporal changes of water column structure and biological productivity that enhanced our understanding of marine biophysical interactions.

Our float observations revealed a physical mechanism that may have enhanced annual primary productivity in the oligotrophic subtropical frontal areas. We found that secondary circulation could have led to a rapid increase of phytoplankton in the upper euphotic zone, where light conditions were improved by strong stratification, and could have introduced water with high nutrient concentrations into the lower part of the euphotic zone or just below the euphotic zone. Satellite chlorophyll images indicated that submesoscale cyclonic eddies could have enhanced primary production near the sea surface. We speculated that the small peaks of CHLA and POC at depths of 100–200 m corresponded to downwelling in a secondary circulation cell that was similar to the effect of the mixed layer pump in the eutrophic subarctic ocean. Such secondary circulation can occur where water masses with different densities are located adjacent to each other when conditions are suitable, regardless of season. While the increase of phytoplankton in the surface layer (McKee et al., 2023) and particle transport to the subsurface layers (Omand et al., 2015) were important, nutrient transport near the euphotic zone shown in this study was also an important factor that may have increased the primary production of this oligotrophic area.

Our study was conducted from January to April 2018, when the Kuroshio had formed a large meander (starting in August 2017) that extended to the east (Qiu et al., 2023). This meandering behavior of the Kuroshio Current may have caused the water column structure to be more spatially diverse during the study period than during periods of no meandering. If this diversity of the structure of the water column caused by active frontogenesis led to an increase of the nutrient supply and primary production in the euphotic zone, the effect should be apparent in historical observations (e.g., satellite chlorophyll observations and moored sediment trap experiments). The supply of nutrients to the surface induced by 3-D secondary circulation in frontal regions as well as the adaptation of phytoplankton (increase of the POC/CHLA ratio) to bright sunlight have been simulated with models (Lapeyre & Klein, 2006; Lévy et al., 2012), but the low spatial resolution of observational data has made validation difficult. By analyzing daily profiles from two closely spaced BGC-Argo floats, we were able to provide evidence for the increase of primary production and nutrient upwelling stimulated by ageostrophic secondary circulation that had been predicted previously by numerical models.

Finally, Kouketsu et al. (2016) have observed increased oxygen concentrations around a cyclonic eddy in the oligotrophic subtropical North Pacific during summer by using 18 BGC-Argo floats and have diagnosed the existence of secondary circulation. Qiu et al. (2006) and Sukigara et al. (2011) have speculated that there is enhanced mixing at the top of subtropical mode water after subduction that could result in the enhancement of primary productivity through transport of nutrients into the euphotic zone. Nutrients transported near the euphotic zone by secondary circulation might eventually be used for primary production and thereby increase the primary productivity in this area. However, this study was unable to clarify the impact of this productivity on annual net primary productivity, most of which depends on winter mixing. In order to evaluate the impact of this process on primary productivity, BGC data sets with high spatiotemporal resolution will be necessary for this area. Future BGC-Argo float observations would greatly facilitate improved understanding of the biological responses and material transport associated with the complex dynamics of water mass structures.

Data Availability Statement

The data of two BGC Argo floats used in this study are released as Argo data. The data of floats including them were collected and made freely available by the International Argo Program and the national programs that contribute to it (https://argo.ucsd.edu, https://ocean-ops.org/). The data can be accessed at the GDAC ftp site (ftp.ifremer.fr/ifremer/argo) or GDAC https sites (https://data-argo.ifremer.fr or https://usgodae.org/pub/outgoing/argo/). Colormaps used in Figures 6, 8 and 12 are available in https://matplotlib.org/cmocean/.

Acknowledgments
We thank the captain, crew, and scientists of the R/V Shinsei-maru of the Japan Agency for Marine-Earth Science and Technology. We also thank S. Oshitani, K. Katayama, and H. Tamada at Marine Works Japan, Ltd. for their analysis and deck work. We thank M. Murata for the nutrient analyses. This study was supported by Grants-in-Aid for Scientific Research on Innovative Areas (Ministry of Education, Culture, Sports, Science and Technology (MEXT) KAKENHI JP15H05818 and JP15K21710). T. Nagai was supported by Grants-in-Aid for Scientific Research (MEXT KAKENHI JP16H01590, JP18H04914, JP19H01965, and JP20K20634). A. J. Fassbender and Y. Takeshita were supported by the David and Lucile Packard Foundation/MBARI. A. J. Fassbender received additional support from NOAA's Pacific Marine Environmental Laboratory. This is PMEL contribution # 5281. This study was performed using the "Joint Research" facility of the Institute for Space-Earth Environmental Research, Nagoya University.

References

Argo. (2000). *Argo float data and metadata from global data assembly centre (Argo GDAC)*. SEANOE. https://doi.org/10.17882/42182

Behrenfeld, M. J. (2010). Abandoning Sverdrup's critical depth hypothesis on phytoplankton blooms. *Ecology*, *91*(4), 977–989. https://doi.org/10.1890/09-1207.1

Behrenfeld, M. J., & Falkowski, P. G. (1997). Photosynthetic rates derived from satellite-based chlorophyll concentration. *Limnology & Oceanography*, *42*, 1–20. https://doi.org/10.4319/lo.1997.42.1.0001

Behrenfeld, M. J., O'Malley, R. T., Boss, E. S., Westberry, T. K., Graff, J. R., Halsey, K. H., et al. (2015). Revaluating ocean warming impacts on global phytoplankton. *Nature Climate Change*, *6*(3), 323–330. https://doi.org/10.1038/NCLIMATE2838

Bishop, J. K. B., & Wood, T. J. (2008). Particulate matter chemistry and dynamics in the twilight zone at VERTIGO ALOHA and K2 sites. *Deep-Sea Research I*, *55*(12), 1684–1706. https://doi.org/10.1016/j.dsr.2008.07.012

Boyd, P. W., Claustre, H., Levy, M., Siegel, D. A., & Weber, T. (2019). Multi-faced particle pumps drive carbon sequestration in the ocean. *Nature*, *568*(7752), 327–335. https://doi.org/10.1038/s41586-019-1098-2

Briggs, N., Perry, M. J., Cetinić, I., Lee, C., D'Asaro, E., Gray, A. M., & Rehm, E. (2011). High-resolution observations of aggregate flux during a sub-polar North Atlantic spring bloom. *Deep-Sea Research I*, *58*(10), 1031–1039. https://doi.org/10.1016/j.dsr.2011.07.007

Cetinić, I., Perry, M. J., Briggs, N. T., Kallin, E., D'Asaro, E. A., & Lee, C. M. (2012). Particulate organic carbon and inherent optical properties during 2008 North Atlantic bloom experiment. *Journal of Geophysical Research (Oceans)*, *117*(C6), C06028. https://doi.org/10.1029/2011JC007771

Chavez, F. P., Messié, M., & Pennington, J. T. (2011). Marine primary production in relation to climate variability and change. *Annual Review of Marine Science*, *3*, 227–260. https://doi.org/10.1146/annurev.marine.010908.163917

Chiswell, S. M. (2011). Annual cycles and spring blooms in phytoplankton: Don't abandon sverdrup completely. *Marine Ecology Progress Series*, *443*, 39–50. https://doi.org/10.3354/meps09453

Cullen, J. J. (1982). The deep chlorophyll maximum: Comparing vertical profiles of chlorophyll a. *Canadian Journal of Fisheries and Aquatic Sciences*, *39*(5), 791–803. https://doi.org/10.1139/f82-108

Dall'Olmo, G., Dingle, J., Polimene, L., Brewin, R. J. W., & Claustre, H. (2016). Substantial energy input to the mesopelagic ecosystem from the seasonal mixed layer pump. *Nature Geoscience*, *9*(11), 820–823. https://doi.org/10.1038/NGEO2818

de Boyer Montégut, C., Madec, G., Fischer, A. S., Lazar, A., & Iudicone, D. (2004). Mixed layer depth over the global ocean: An examination of profile data and a profile-based climatology. *Journal of Geophysical Research (Oceans)*, *109*(C12), C12003. https://doi.org/10.1029/2004JC002378

Ducet, N., Le Traon, P. Y., & Reverdin, G. (2000). Global high-resolution mapping of ocean circulation from the combination of T/P and ERS-1/2. *Journal of Geophysical Research (Oceans)*, *105*(C8), 19477–19498. https://doi.org/10.1029/2000jc900063

Fischer, A. D., Moberg, E. A., Alexander, H., Brownlee, E. F., Hunter-Cevera, K. R., Pitz, K. J., et al. (2014). Sixty years of sverdrup: A restrospective of progress in the study of phytoplankton blooms. *Oceanography*, *27*(1), 222–235. https://doi.org/10.5670/oceanog.2014.26

Fox-Kemper, B., Ferrari, R., & Hallberg, R. (2008). Parameterization of mixed layer eddies. Part I: Theory and diagnosis. *Journal of Physical Oceanography*, *38*(6), 1145–1165. https://doi.org/10.1175/2008JPO3792.1

Fujiki, T., Sasaoka, K., Matsumoto, K., Wakita, M., & Mino, Y. (2016). Seasonal variability of phytoplankton community structure in the subtropical Western North Pacific. *Journal of Oceanography*, *72*(3), 343–358. https://doi.org/10.1007/s10872-015-0346-9

Garcia, H. E., & Gordon, L. I. (1992). Oxygen solubility in seawater: Better fitting equations. *Limnology & Oceanography*, *37*(6), 1129–1343. https://doi.org/10.4319/lo.1992.37.6.1307

Geider, R. J. (1987). Light and temperature dependence of the carbon and chlorophyll a ratio in microalgae and cyanobacteria: Implications for physiology and growth of phytoplankton. *New Phytologist*, *106*(1), 1–34. https://doi.org/10.1111/j.1469-8137.1987.tb04788.x

Gill, A. E. (1982). *Atmosphere-ocean dynamics* (p. 680). Academic Press.

Graff, J. R., & Behrenfeld, M. J. (2018). Photoacclimation responses in subarctic Atlantic phytoplankton following a natural mixing-restratification event. *Frontiers in Marine Science*, *5*, 209. https://doi.org/10.3389/fmars.2018.00209

Grasshoff, K. (1976). *Methods of seawater analysis* (p. 317pp). Verlag Chemie.

Honda, M. C., Wakita, M., Matsumoto, K., Fujiki, T., Siswanto, E., Sasaoka, K., et al. (2017). Comparison of carbon cycle between the Western Pacific subarctic and subtropical time-series stations: Highlights of the K2S1 project. *Journal of Oceanography*, *73*(5), 647–667. https://doi.org/10.1007/s10872-017-0423-3

Hoskins, B. J., Draghici, I., & Davies, H. C. (1978). A new look at the ω-equation. *Quarterly Journal of the Royal Meteorological Society*, *104*(439), 31–38. https://doi.org/10.1002/qj.49710443903

Hoskins, B. J., & Pedder, M. A. (1980). The diagnosis of middle latitude synoptic development. *Quarterly Journal of the Royal Meteorological Society*, *106*(450), 707–719. https://doi.org/10.1256/smsqj.45003

Irwin, A. J., & Oliver, M. J. (2009). Are ocean deserts getting larger? *Geophysical Research Letters*, *36*(18), L18609. https://doi.org/10.1029/2009GL2009GL039883

Japan Meteorological Agency. (1999). The manual on oceanographic observation part 1. *Japan Meteorological Agency*, 200. (in Japanese).

Johnson, K., Pasquenron de Fommervault, O., Serra, R., D'Ortenzio, F., Schmechtig, C., Claustre, H., & Poteau, A. (2016). Processing bio-argo nitrate concentration at the DAC level. https://doi.org/10.13155/46121

Johnson, K. S., Plant, J. N., Coletti, L. J., Jannasch, H. W., Sakamoto, C. M., Riser, S. C., et al. (2017). Biogeochemical sensor performance in the SOCCOM profiling float array. *Journal of Geophysical Research (Oceans)*, *122*(8), 6416–6436. https://doi.org/10.1002/2017JC012838

Johnson, K. S., Riser, S. C., & Karl, D. M. (2010). Nitrate supply from deep to near surface waters of the North Pacific subtropical gyre. *Nature*, *465*(7301), 1062–1065. https://doi.org/10.1038/nature09170

Kouketsu, S., Inouem, R., & Suga, T. (2016). Western North Pacific Integrated Physical-Biogeochemical Ocean Observation Experiment (INBOX): Part 3. Mesoscale variability of dissolved oxygen concentrations observed by multiple floats during S1-INBOX. *Journal of Marine Research*, *74*(2), 101–131. https://doi.org/10.1357/002224016819257326

Lacour, L., Briggs, N., Claustre, H., Ardyna, M., & Dall'Olmo, G. (2019). The intraseasonal dynamics of the mixed layer pump in the subpolar North Atlantic Ocean: A biogeochemical-Argo float approach. *Global Biogeochemical Cycles*, *33*(3), 266–281. https://doi.org/10.1029/2018GB005997

Lapeyre, G., & Klein, P. (2006). Impact of the small-scale elongated filaments on the Oceanic vertical pump. *Journal of Marine Research*, *64*(6), 835–851. https://doi.org/10.1357/00222400677968369

Legal, C., Klein, P., Tréguier, A.-M., & Paillet, J. (2007). Diagnosis of the vertical motions in a mesoscale stirring regime. *Journal of Physical Oceanography*, *37*, 1413–1424. https://doi.org/10.1175/JPO3053.1

Lévy, M., Iovino, D., Resplandy, L., Klein, P., Madec, G., Tréguier, A.-M., et al. (2012). Large-scale impacts of submesoscale dynamics on phytoplankton: Local and remote effects. *Ocean Modelling*, *43–44*, 77–93. https://doi.org/10.1016/j.ocemod.2011.12.003

Mahadevan, A., D'Asaro, E., Lee, C., & Perry, M. J. (2012). Eddy-driven stratification initiates North Atlantic spring phytoplankton blooms. *Science*, *337*(6090), 54–58. https://doi.org/10.1126/science.1218740

Matsumoto, K., Abe, O., Fujiki, T., Sukigara, C., & Mino, Y. (2016). Primary productivity at the time-series stations in the northwestern Pacific Ocean: Is the subtropical station unproductive? *Journal of Oceanography*, *72*(3), 359–371. https://doi.org/10.1007/s10872-016-0354-4

Matsumoto, K., Sasai, Y., Sasaoka, K., Siswanto, E., & Honda, M. C. (2021). The formation of subtropical phytoplankton blooms is dictated by water column stability during winter and spring in the oligotrophic northwestern North Pacific. *Journal of Geophysical Research (Oceans)*, *126*(4), e2020JC016864. https://doi.org/10.1029/2020JC016864

Maurer, T. L., Plant, J. N., & Johnson, K. S. (2021). Delayed-Mode quality control of oxygen, nitrate, and pH data on SOCCOM biogeochemical profiling floats. *Frontiers in Marine Science*, *8*, 683207. https://doi.org/10.3389/fmars.2021.683207

McKee, D. C., Doney, S. C., Penna, A. D., Boss, E. A., Gaube, P., & Behrenfeld, M. J. (2023). Biophysical dynamics at ocean fronts revealed by bio-Argo floats. *Journal of Geophysical Research (Oceans)*, *128*(3), e2022JC019226. https://doi.org/10.1029/2022JC019226

Mino, Y., Sukigara, C., Hawakami, H., Wakita, M., & Honda, M. C. (2023). Mesopelagic particulate nitrogen dynamics in the subarctic and subtropical regions of the Western North Pacific. *Frontiers in Earth Science*, *11*, 1176889. https://doi.org/10.3389/feart.2023.1176889

Morel, A., & Ahn, Y. H. (1991). Optics of heterotrophic nanoflagellates and ciliates: A tentative assessment of their scattering role in Oceanic waters compared to those of bacterial and algal cells. *Journal of Marine Research*, *49*(1), 177–202. https://doi.org/10.1357/002224091784968639

Morel, A., Huot, Y., Gentili, B., Werdell, P. J., Hooker, S. B., & Franz, B. A. (2007). Examining the consistency of products derived from various ocean color sensors in open ocean (case 1) waters in the perspective of a multi-sensor approach. *Remote Sensing of Environment*, *111*(1), 69–88. https://doi.org/10.1016/j.rse.2007.03.012

Nagai, T., & Clayton, S. (2017). Nutrient interleaving below the mixed layer of the Kuroshio Extension front. *Ocean Dynamics*, *67*(8), 1027–1046. https://doi.org/10.1007/s10236-017-1070-3

Omand, M. M., D'Asaro, E. A., Lee, C. M., Perry, M. J., Briggs, N., Cetinić, I., & Mahadevan, A. (2015). Eddy-Deiven subduction exports particulate organic carbon from the spring bloom. *Science*, *348*(6231), 222–225. https://doi.org/10.1126/science.1260062

Qiu, B., Chen, S., & Oka, E. (2023). Why did the 2017 Kuroshio large meander event become the longest in the past 70 years? *Geophysical Research Letters*, *50*(10), e2023GL103548. https://doi.org/10.1029/2023GL103548

Qiu, B., Hacker, P., Chen, S., Donohue, K. A., Watts, D. R., Mitsudera, H., et al. (2006). Observation of the subtropical mode water evolution from the Kuroshio extension system study. *Journal of Physical Oceanography*, *36*(3), 457–473. https://doi.org/10.1175/JPO2849.1

Redfiled, A. C., Ketchum, B. H., & Richards, F. A. (1963). The influence of organisms on the composition of sea water. In M. N. Hill (Ed.), *The sea* (Vol. 2, pp. 26–77). Wiley Interscience.

Rembauville, M., Briggs, N., Ardyna, M., Uitz, J., Catala, P., Penkerch, C., et al. (2017). Plankton assemblage estimated with BGC-Argo floats in the Southern Ocean: Implications for seasonal successions and particle export. *Journal of Geophysical Research (Oceans)*, *122*(10), 8278–8292. https://doi.org/10.1002/2017JC013067

Sasai, Y., Yoshikawa, C., Lan Smith, S., Hashioka, T., Matsumoto, K., Wakita, M., et al. (2016). Coupled 1-D physical–biological model study of phytoplankton production at two contrasting time-series stations in the Western North Pacific. *Journal of Oceanography*, *72*(3), 509–526. https://doi.org/10.1007/s10872-015-0341-1

Schallenberg, C., Harley, J. W., Jansen, P., Davies, D. M., & Trull, T. W. (2019). Multi-year observations of fluorescence and backscatter at the Southern Ocean Time Series (SOTS) shed light on two distinct seasonal bio-optical regimes. *Frontiers in Marine Science*, *6*, 595. https://doi.org/10.3389/fmars.2019.00595

Siegel, D. A., Doney, S. C., & Yoder, J. A. (2002). The North Atlantic spring phytoplankton bloom and Sverdrup's critical depth hypothesis. *Science*, *296*(5568), 730–733. https://doi.org/10.1126/science.1069174

Siswanto, E., Matsumoto, K., Honda, M. C., Fujiki, T., Sasaoka, K., & Saino, T. (2015). Reappraisal of meridional differences of factors controlling phytoplankton biomass and initial increase preceding seasonal bloom in the northwestern Pacific Ocean. *Remote Sensing of Environment*, *159*, 44–56. https://doi.org/10.1016/j.rse.2014.11.028

Sukigara, C., Suga, T., Saino, T., Toyama, K., Yanagimoto, D., Hanawa, H., & Shikama, N. (2011). Biogeochemical evidence of large diapycnal diffusivity associated with the subtropical mode water of the North Pacific. *Journal of Oceanography*, *67*(1), 77–85. https://doi.org/10.1007/s10872-011-008-5

Sukigara, C., Suga, T., Toyama, K., & Oka, E. (2014). Biogeochemical responses associated with the passage of a cyclonic eddy based on shipboard observations in the Western North Pacific. *Journal of Oceanography*, *70*(5), 435–445. https://doi.org/10.1007/s10872-014-0244-6

Sverdrup, H. U. (1953). On conditions for the vernal blooming of phytoplankton. *ICES Journal of Marine Science*, *18*(3), 287–295. https://doi.org/10.1093/icesjms/18.3.287

Takeshita, Y., Martz, T. R., Johnson, K. S., Plant, J. N., Gilbert, D., Riser, S. C., et al. (2013). A climatology-based quality control procedure for profiling float oxygen data. *Journal of Geophysical Research (Oceans)*, *118*(10), 5640–5650. https://doi.org/10.1002/jgrc.20399

Taylor, A. H., Geider, R. J., & Gilbert, F. J. (1997). Seasonal and latitudinal dependencies of plankton carbon-to-chlorophyll *a* ratios: Results of a modelling study. *Marine Ecology Progress Series*, *152*, 51–66. https://doi.org/10.3354/meps152051

Taylor, J. R., & Ferrari, R. (2011). Shutdown of turbulent convection as a new criterion for the onset of spring phytoplankton blooms. *Limnology & Oceanography*, *56*(6), 2293–2307. https://doi.org/10.4319/lo.2011.56.6.2293

Thierry, V., Bittig, H., Gilbert, D., Kobayashi, T., Sato, K., & Schmid, C. (2018). Processing Argo OXYGEN data at the DAC level, v2.3.1. https://doi.org/10.13155/39795

Wakita, M., Honda, M. C., Matsumoto, K., Fujiki, T., Kawakami, H., Yasunaka, S., et al. (2016). Biological organic carbon export estimated from the annual carbon budget observed in the surface waters of the Western subarctic and subtropical North Pacific Ocean from 2004 to 2013. *Journal of Oceanography*, *72*(5), 665–685. https://doi.org/10.1007/s10872-016-0379-8

Wong, A., & Keeley, R. (2020). *Carval and the argo data management team*. Argo Quality Control Manual for CTD and Trajectory Data. https://doi.org/10.13155/33951

Xiao, S., Zhang, L., Teng, Y., Huang, T., & Luo, W. (2021). The particulate organic carbon-to-nitrogen ratio varies with ocean currents. *Frontiers in Environmental Science*, *9*, 757471. https://doi.org/10.3389/fenvs.2021.757471

Zhang, Z., Qiu, B., Klein, P., & Travis, S. (2019). The influence of geostrophic strain on Oceanic ageostrophic motion and surface chlorophyll. *Nature Communications*, *10*(2838), 1–11. https://doi.org/10.1038/s41467-019-10883-w